Cell Reports

Report

Huntingtin Aggregation Impairs Autophagy, Leading to Argonaute-2 Accumulation and Global MicroRNA Dysregulation

Graphical Abstract

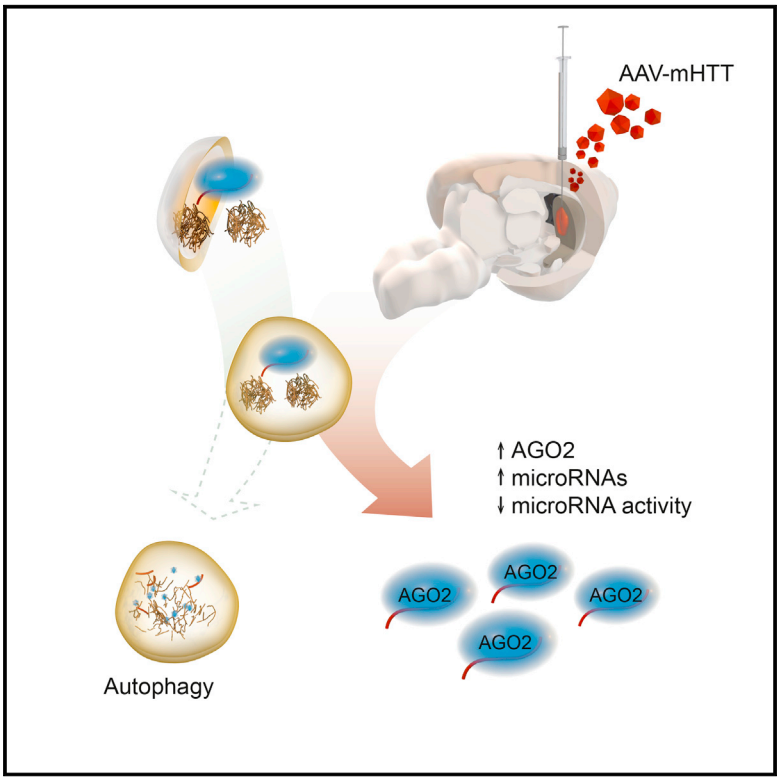

Authors

Karolina Pircs, Rebecca Petri, Sofia Madsen, ..., Malin Parmar, Roger A. Barker, Johan Jakobsson

Correspondence

johan.jakobsson@med.lu.se

In Brief

Pircs et al. report that aggregation of the mutant huntingtin protein, a hallmark of Huntington's disease proteinopathy, impairs macroautophagy, leading to Argonaute-2 accumulation and global dysregulation of microRNAs. These results indicate that autophagy not only influences protein aggregation but also directly contributes to the global alterations of post-transcriptional networks in Huntington's disease.

Highlights

- Mutant HTT overexpression causes impairment of autophagy, resulting in AGO2 accumulation
- Activation of autophagy reverses AGO2 accumulation in neurons
- AGO2 accumulation results in a global increase in miRNA levels
- AGO2 re-localizes to stress granules, resulting in loss of miRNA activity

Data and Software Availability

GSE78928

Pircs et al., 2018, Cell Reports *24*, 1397–1406
August 7, 2018
https://doi.org/10.1016/j.celrep.2018.07.017

CellPress

Cell Reports
Report

Huntingtin Aggregation Impairs Autophagy, Leading to Argonaute-2 Accumulation and Global MicroRNA Dysregulation

Karolina Pircs,[1] Rebecca Petri,[1] Sofia Madsen,[1] Per Ludvik Brattås,[1] Romina Vuono,[2] Daniella R. Ottosson,[3] Isabelle St-Amour,[4] Bob A. Hersbach,[1] Monika Matusiak-Brückner,[1] Sofia Hult Lundh,[5] Åsa Petersén,[5] Nicole Déglon,[6] Sébastien S. Hébert,[4] Malin Parmar,[3] Roger A. Barker,[2,3] and Johan Jakobsson[1,7,*]

[1]Laboratory of Molecular Neurogenetics, Department of Experimental Medical Science, Wallenberg Neuroscience Center and Lund Stem Cell Center, BMC A11, Lund University, 221 84 Lund, Sweden

[2]John van Geest Centre for Brain Repair and Department of Neurology, Department of Clinical Neurosciences, University of Cambridge, Forvie Site, Cambridge CB2 0PY, UK

[3]Developmental and Regenerative Neurobiology, Department of Experimental Medical Science, Wallenberg Neuroscience Center and Lund Stem Cell Center, BMC A11, Lund University, 221 84 Lund, Sweden

[4]Axe Neurosciences, Centre de Recherche du CHU de Québec – Université Laval, CHUL, Québec, QC G1V 4G2, Canada

[5]Translational Neuroendocrine Research Unit (TNU), Department of Experimental Medical Science, Wallenberg Neuroscience Center, BMC D11, Lund University, 221 84 Lund, Sweden

[6]Laboratory of Cellular and Molecular Neurotherapies (LCMN), Department of Clinical Neuroscience (DNC), Neuroscience Research Center (CRN), Lausanne University Hospital (CHUV), 1011 Lausanne, Switzerland

[7]Lead Contact

*Correspondence: johan.jakobsson@med.lu.se

https://doi.org/10.1016/j.celrep.2018.07.017

SUMMARY

Many neurodegenerative diseases are characterized by the presence of intracellular protein aggregates, resulting in alterations in autophagy. However, the consequences of impaired autophagy for neuronal function remain poorly understood. In this study, we used cell culture and mouse models of huntingtin protein aggregation as well as post-mortem material from patients with Huntington's disease to demonstrate that Argonaute-2 (AGO2) accumulates in the presence of neuronal protein aggregates and that this is due to impaired autophagy. Accumulation of AGO2, a key factor of the RNA-induced silencing complex that executes microRNA functions, results in global alterations of microRNA levels and activity. Together, these results demonstrate that impaired autophagy found in neurodegenerative diseases not only influences protein aggregation but also directly contributes to global alterations of intracellular post-transcriptional networks.

INTRODUCTION

MicroRNAs (miRNAs) are small non-coding RNAs that provide post-transcriptional control of gene expression. miRNAs play an important role in the brain, where hundreds of different miRNAs are expressed and thought to regulate thousands of transcripts (Petri et al., 2014). Several lines of evidence indicate that miRNAs are likely to play an important role in neurodegenerative diseases (NDDs) (Maciotta et al., 2013). For example, conditional deletion of *Dicer*, a key enzyme in the miRNA biogenesis pathway, results in neuronal cell death (Pang et al., 2014). In addition, there are numerous reports describing changes in miRNA expression levels in NDDs such as Alzheimer's disease (AD), Parkinson's disease (PD), Huntington's disease (HD), and amyotrophic lateral sclerosis (ALS) (Maciotta et al., 2013). It is therefore likely that alterations in miRNA levels participate in the pathophysiological events underlying cell dysfunction and loss in these diseases.

AD, PD, HD, ALS, and other diseases form a large class of NDDs known as proteinopathies, characterized by the formation of specific protein aggregates in the brain. Neurons appear to be particularly sensitive to aggregation-prone proteins, indicating that neuronal survival is highly dependent on maintaining efficient protein quality control with rapid removal of toxic and aggregated proteins (Cortes and La Spada, 2014). However, it remains unclear how protein aggregation influences intracellular functions and why specific neuronal subtypes ultimately are lost in these different disorders. For example, it is well established that neuronal gene expression programs are severely altered in these disorders, but mechanistic insight into how neuronal protein aggregation results in selective disturbances in transcriptional networks is currently lacking.

Macroautophagy (hereafter referred to as autophagy) is an evolutionary conserved lysosomal degradation pathway characterized by the formation of an autophagosome, a double-membraned vesicle that isolates the cytoplasmic cargo for destruction (Martin et al., 2015). The autophagosome ultimately fuses with a lysosome, forming the autolysosome where the cargo is degraded. Several studies have documented altered autophagy in NDDs, and boosting autophagy has been proposed as a novel therapeutic strategy (Martin et al., 2015). In addition to clearing toxic and misfolded

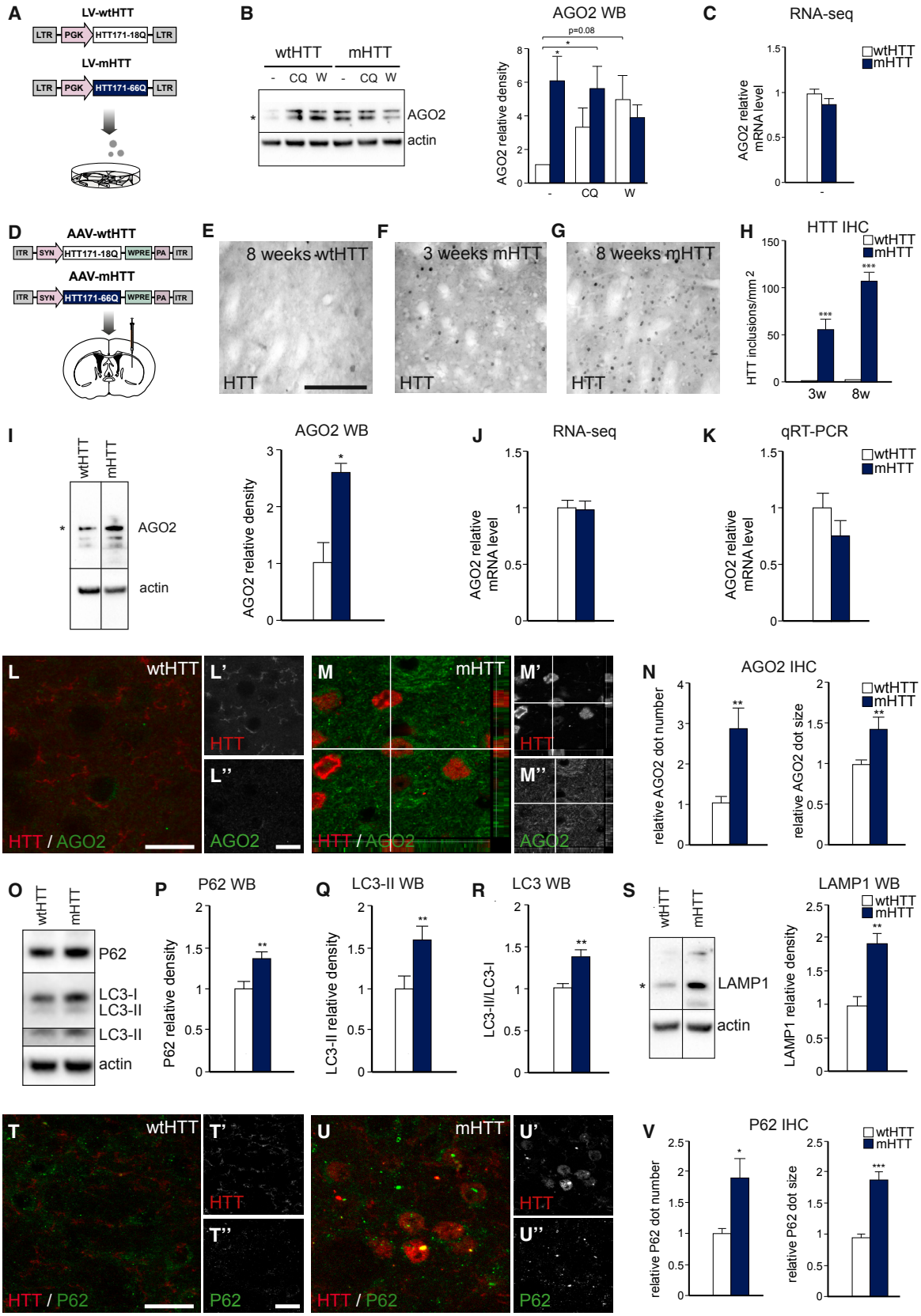

(legend on next page)

proteins, we and others have recently found that autophagy also plays a critical role in maintaining brain homeostasis through selective protein degradation (Petri et al., 2017; Yamamoto and Yue, 2014). One possibility is therefore that alterations of autophagy in NDDs also directly influence other intracellular neuronal functions.

One protein that is of interest in this regard is Argonaute-2 (AGO2), which is degraded by selective autophagy under basal conditions (Gibbings et al., 2012). AGO2 is a core component of the RNA-induced silencing complex (RISC), which executes miRNA functions. In the RISC, AGO2 has multiple roles, including biogenesis and maturation of miRNAs, as well as direct binding of mature miRNAs (Petri et al., 2014). AGO2 also provides endoribonuclease activity that enables direct degradation of miRNA target transcripts, as well as recruitment of other downstream factors that mediate transcriptional repression or decay (Bossé and Simard, 2010). Several studies have shown that intracellular AGO2 protein is carefully titrated at a post-transcriptional level and that miRNA-free AGO2 is degraded through a specific mechanism (Füllgrabe et al., 2014). Removal of mature miRNAs by deleting the miRNA biogenesis factors *Dgcr8* or *Dicer* results in a parallel reduction of AGO2 protein levels (Gibbings et al., 2012; Savas et al., 2008). Furthermore, overexpression of AGO2 is very difficult to achieve, further suggesting a feedback regulation of AGO2 protein levels (Füllgrabe et al., 2014; He et al., 2012). Together, these observations indicate that the regulation of intracellular AGO2 protein levels is critical in maintaining appropriate miRNA activity.

In this study, we used both cell culture and mouse models as well as post-mortem material from patients with HD to demonstrate that AGO2 accumulates as a result of impaired autophagy in neurons expressing aggregating mutant Huntingtin (mHTT). This AGO2 accumulation results in a global alteration of miRNA activity. Our results provide mechanistic insights into how impairment in autophagy in NDDs contributes to dysregulation of miRNA networks.

RESULTS

mHTT-Mediated Impairment of Autophagy Correlates with Accumulation of AGO2

To investigate a potential link between alterations in autophagy in NDDs and AGO2 expression levels, we transduced 293T cells with lentiviral vectors expressing exon 1 of wild-type *HTT* (*wtHTT*, 18 polyQ repeats) or mutant *HTT* (*mHTT* 66Q, 66 polyQ repeats) (Figure 1A). *HTT* is mutated in HD, where a polyglutamine expansion in the first exon ultimately leads to a toxic gain of function for *mHTT* and protein aggregation (DiFiglia et al., 1997). Vector transduction was also combined with chloroquine (CQ) treatment, which prevents both the fusion of the autophagosome with the lysosome and lysosomal protein degradation, or with wortmannin (W) treatment, a phosphatidylinositol 3-kinase (PI3K) inhibitor that provides an early block of autophagy and inhibits microtubule-associated protein 1A/1B-light chain 3 (LC3) lipidation. Using this system, we monitored autophagic activity by assessing the levels of LC3II, LC3-II/ I ratio, p62, and LAMP1 using western blot (WB) and immunocytochemistry (ICC) and found, in line with other studies (Martin et al., 2015), that expression of mHTT mediates a late-step block of autophagy characterized by failure of fusion of the autophagosome and the lysosome (Figures S1A–S1R).

We next investigated AGO2 expression levels using WB in 293T cells transduced with mHTT. We found a significant increase in the AGO2 protein level compared to wtHTT-expressing cells, whereas there was no difference in the AGO2 mRNA level (Figures 1B, 1C, and S1S). A similar increase in AGO2 protein was also seen in wtHTT-transduced cells when we inhibited autophagy using CQ or W (Figures 1B, 1C, and S1S), whereas we found no additive effect of mHTT expression after CQ or W treatment. Together, these data demonstrate that mHTT-mediated autophagy impairment results in accumulation of AGO2 at a post-transcriptional stage in mHTT-expressing cells in a manner similar to that seen following chemical autophagy inhibition.

Figure 1. mHTT Expression Alters Autophagy and Results in Accumulation of AGO2 *In Vitro* and *In Vivo*

(A) Diagrams of the lentivrus (LV)-*mHTT* and LV-*wtHTT* vectors and the experimental workflow, showing transduction of 239T cells before assays.

(B) There was an elevated expression of AGO2 protein in mHTT-expressing cells. AGO2 protein levels increased after autophagic impairment induced by CQ or W in LV-wtHTT-overexpressing cells. AGO2 protein is marked with an asterisk. n = 5.

(C) There was no change in the mRNA level of the AGO2 protein in LV-mHTT- or LV-wtHTT-expressing 293T cells. n = 3.

(D) Diagrams of the AAV-*mHTT* and AAV-*wtHTT* vectors and the experimental workflow.

(E–H) Time-dependent accumulation of HTT was present in AAV-*mHTT* injected animals after 3 (F) and 8 (G) weeks, but not in AAV-*wtHTT* (E)-injected animals. (H) Number of HTT aggregates/ mm^2. n = 45 (3 animals/ group).

(I) AGO2 protein accumulates after 3 weeks in AAV-*mHTT*-injected animals. AGO2 protein is marked with an asterisk. n = 8 (4 animals/ group).

(J) AGO2 mRNA levels were not changed 3 weeks after mHTT overexpression. n = 3.

(K) Relative AGO2 mRNA levels were not changed 3 weeks after mHTT overexpression. n = 5.

(L–N) AGO2 protein accumulates in AAV-*mHTT* (M), but not in AAV-*wtHTT* (L)-injected animals 8 weeks after injection. (N) There were significantly more, as well as bigger puncta in the AAV-*mHTT*-injected mice than in those injected with AAV-*wtHTT*. n = 27 (3 animals/ group).

(O–R) WB autophagic protein expression levels in AAV-*mHTT* and *wtHTT*-injected animals (O). Increased expression levels of the autophagic markers p62 (P) and LC3-II (Q) and LC3-II/LC3-I ratio (R) are detected 3 weeks after AAV-*mHTT* injections. n = 8 (4 animals/ group).

(S) Accumulation of LAMP1 was seen after 3 weeks in AAV-*mHTT*-injected but not in AAV-*wtHTT*-injected mice. LAMP1 is marked with an asterisk. n = 10 and 20 for wtHTT and mHTT, respectively (4 animals/ group).

(T–V) IHC demonstrate p62 accumulation in the AAV-*mHTT* (U) compared to AAV-*wtHTT* (T)-injected animals. (V) Relative p62 dot number and size were significantly increased in mHTT-overexpressing animals compared to wtHTT 8 weeks after injection. n = 19 and 24 for AAV-*wtHTT*- and AAV-*mHTT*-injected animals, respectively (3 animals/ group).

WB values were normalized to LV-wtHTT non-treated (B) or AAV-wtHTT (I and O–S) expression levels and corrected to actin values. ***$p < 0.001$, **$p < 0.01$, *$p < 0.05$; nonparametric Kruskal-Wallis test was used for (B); two-tailed two-sample unequal variance t tests were used for all other cases. All data are shown as mean ± SEM. Scale bars represent 50 μm (E–G), 10 μm (L and M), and 10 μm (T and U). See also Figures S1–S3 and S6 and Tables S1 and S3.

AGO2 Accumulates in Striatal Neurons Expressing mHTT

The most affected neuronal cell type in HD is medium spiny neurons in the striatum. To study the role of mHTT in modulating autophagy and AGO2 levels in striatal neurons *in vivo*, we generated adeno-associated viral (AAV) vectors expressing either exon 1 *wtHTT* or *mHTT* under the control of the neuron-specific synapsin promoter that were subsequently injected into the striatum of the mouse brain (Figure 1D). Mice injected with AAV-*mHTT* showed a progressive increase in intracellular mHTT inclusions, whereas AAV-*wtHTT* did not develop such inclusions (Figures 1E–1H). We also found progressive loss of DARPP-32 levels in AAV-*mHTT*-injected mice in the absence of neuronal cell loss, indicating progressive dysfunction of striatal medium spiny neurons (Figures S2A–S2E).

We next investigated AGO2 levels after AAV-*mHTT* injections using WB and found an almost 3-fold increase 3 weeks post-injection (Figure 1I). We did not observe any changes in AGO2 mRNA levels, as monitored by RNA sequencing (RNA-seq) or by qRT-PCR (Figures 1J and 1K). When we investigated AGO2 expression in the striatum using immunohistochemistry (IHC) with two different antibodies, we found cytoplasmic AGO2 protein accumulation in the animals injected with AAV-*mHTT* but not in animals injected with AAV-*wtHTT* (Figures 1L–1N and S3A–S3D). We did not see any colocalization between AGO2 and mHTT aggregates in animals injected with AAV-*mHTT*, suggesting that AGO2 accumulation is not a result of direct binding to HTT aggregates (Figures 1L–1N). We also investigated the level of other AGO proteins in the presence of mHTT but did not find any changes in the protein or mRNA level for AGO1 and AGO4 (Figures S3E–S3G). Together, these data show that expression of mHTT in striatal neurons results in protein aggregation that is associated with formation and accumulation of AGO2 protein puncta.

Activation of Autophagy Reverses AGO2 Accumulation in Striatal Neurons Expressing mHTT

We next investigated alterations in autophagy following AAV-*mHTT* injections in the mouse brain. Using WB and IHC analysis of dissected striatal tissue from mice injected with AAV-*mHTT* and AAV-*wtHTT*, we found increased levels of p62 and LC3-II as well as an increased LC3-II/I ratio, suggesting impaired autophagosome-lysosome fusion or inhibition of lysosome-mediated proteolysis (Figures 1O–1R, S3H, and S3I). We also found an increase in the lysosomal marker LAMP1 (Figures 1S, S3J, and S3K). We found no changes in the mRNA levels of any of these markers, as monitored by RNA-seq (Figures S3L–S3N). Confocal analysis of HTT/p62 co-staining revealed numerous p62-positive mHTT aggregates in AAV-*mHTT* animals (Figures 1T–1V). p62-positive clusters were found to accumulate adjacent to the protein aggregates, with significant p62 sequestration within aggregates (Figure S3O). Although accumulated p62 and AGO2 puncta were often found in the same cells, we never saw colocalization of these two proteins, which is in line with previous data showing that AGO2 is degraded by autophagy in a p62-independent manner (Figures S3P–S3S; Table S1; Gibbings et al., 2012; Savas et al., 2008). In addition, AGO2 puncta never colocalized with the autophagosomal marker LC3 in mHTT-expressing cells, whereas we found several examples of colocalization between AGO2 and LC3 in wtHTT-expressing neurons, indicating that AGO2 is selectively degraded by autophagy in neurons expressing the wt protein but not in neurons expressing the mutant protein (Figures S3T and S3U). Together, these results demonstrate that expression of mHTT leads to a distinct impairment in autophagy that correlates with the accumulation of AGO2.

To provide a mechanistic link between the decrease in autophagy activity and AGO2 accumulation, we next overexpressed Beclin-1 (BECN1), a positive regulator of autophagosome formation, together with mHTT in the mouse brain (Figures S4A and S4B). Three weeks after co-delivery of AAV-*mHTT* and AAV-*BECN1*, the number of p62 aggregates was dramatically lower compared to animals injected with AAV-*mHTT* alone (Figures 2A–2C). We also measured the changes in the level of LC3 with WB and IHC to see whether there was increased autophagy activity and found a significant increase in the level of LC3-II and LC3-II/I ratio (Figure S4C). LC3-positive dots accumulated in the co-injected animals around the mHTT aggregates (Figures S4D and S4E). We did not detect any changes in the level of LAMP1 using IHC or WB, indicating that BECN1 overexpression did not affect the formation and amount of lysosomes or endosomes (Figures S4F–S4I). We also found that BECN1 accumulated around mHTT inclusions, which is in line with its association with newly formed autophagosomes (Figures S4J–S4L).

Strikingly, AGO2 dot number and size were significantly reduced in BECN1 co-expressing mice (Figures 2D–2F). Thus, BECN1 co-overexpression decreased the number of p62 aggregates and reduced AGO2 dot size and number, providing a mechanistic link between autophagy and AGO2 accumulation.

It is worth noting that the number of HTT inclusions was 3 times less in co-injected mice than in animals injected with AAV-*mHTT* only (Figures 2G–2I) and that the DARPP-32 levels in striatal projection neurons were significantly higher (Figure 2J), suggesting that autophagy activation using AAV-*BECN1* interferes with the progression of the mHTT-associated disease phenotype.

AGO2 Accumulation in a HD Mouse Model and Post-mortem HD Tissue

Although the AAV-*mHTT* model is a good tool to study protein aggregation in neurons, it fails to recapitulate many of the features of HD (e.g., pathology in non-neuronal cells). To investigate a potential dysregulation of AGO2 in a more disease-relevant model of HD, we used BACHD mice, which express full-length mHTT with 97 glutamine repeats under the control of endogenous HTT regulatory sequences (Gray et al., 2008). At 6 months of age, which represents an early manifest stage, we found an accumulation of p62 inclusions in striatal neurons of BACHD mice that was not seen in striatal tissue from wt littermates (Figures 3A–3D). We also detected AGO2 accumulation in striatal tissue of BACHD mice but not in controls (Figures 3A–3C and 3E). These AGO2 puncta were primarily found in the cytoplasm of cells with a neuronal morphology. As with the AAV-model, we never saw colocalization of p62 and AGO2 protein, although p62 aggregates and AGO2 puncta were often found in the same cells (Figure 3F; Table S1).

We then performed IHC on post-mortem striatal material from HD patients of different pathological grades and healthy

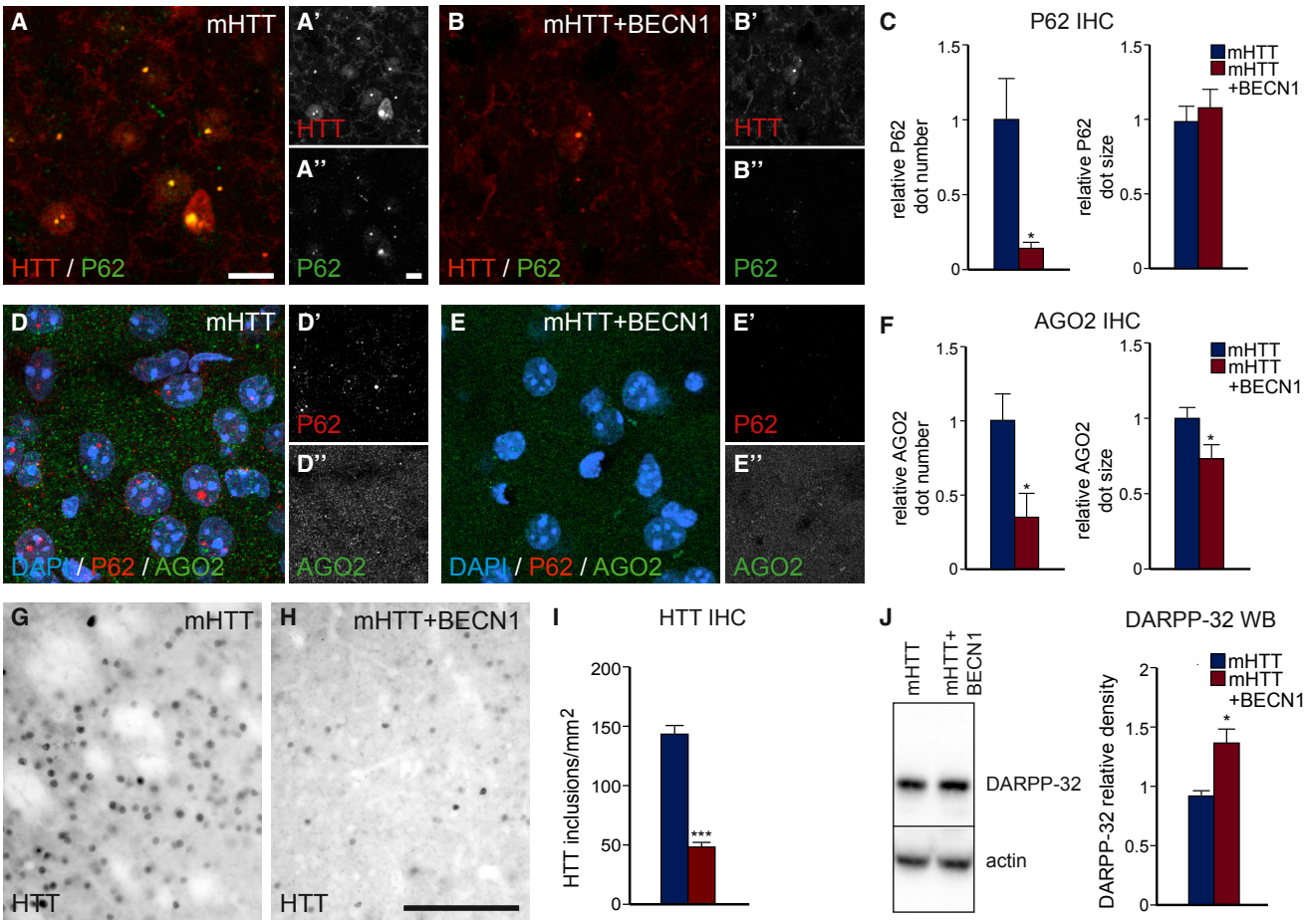

Figure 2. AAV-Mediated Delivery of Beclin1 Reverses mHTT-Associated Phenotypes

(A–C) Co-injection of AAV-*BECN1* and AAV-*mHTT* (B) reversed the aggregation of HTT and p62 compared to AAV-*mHTT* (A)-injected animals. (C) There was a reduction in the number, but not in the size of p62 aggregates. n = 10 (3 animals/group).

(D–F) IHC demonstrate decreased AGO2 accumulation in the co-injected animals (E) compared to the AAV-*mHTT* (D). (F) Overexpression of BECN1 and mHTT significantly decreased AGO2 accumulation in both number and size. n = 10 (3 animals/group).

(G–I) IHC demonstrate decreased HTT aggregation in the co-injected animals (H) compared to the AAV-*mHTT* (G). (I) Overexpression of BECN1 greatly reduced the number of HTT aggregates. n = 41 for AAV-*mHTT*, and n = 61 for AAV-*BECN1*+*mHTT* (3 animals/group).

(J) The DARPP-32 protein level was significantly higher in AAV-*BECN1*-co-injected animals compared to *mHTT*-injected animals. n = 10 (3 animals/group). WB values were normalized to AAV-*mHTT* injection expression levels and corrected to actin values. ***$p < 0.001$, *$p < 0.05$, two-tailed two-sample unequal variance t tests. All data are shown as mean ± SEM. Scale bars represent 37.5 μm (A, B, D, and E) and 50 μm (G and H). See also Figure S4.

age-matched individuals (Table S2). We found AGO2 accumulation in cells in striatal tissue of the HD patients but not in healthy individuals (Figure 3G–3M). We also found accumulation of p62 adjacent to mHTT inclusions in the neurons that were not seen in the striatal tissue of healthy individuals (Figures S5A and S5B). Similarly, we did not see colocalization of p62 and AGO2 protein (Figure 3N; Table S1). These data demonstrate that AGO2 accumulates in a HD mouse model as well as in HD patients.

AGO2 Accumulation Results in a Global Increase in miRNA Levels

AGO2 levels are directly related to the number of mature miRNAs present within a cell (Diederichs and Haber, 2007). This suggests that the increase in AGO2 levels that occurs following mHTT expression may result in an increased level of mature miRNAs, which may be coupled to profound effects on the activity of miRNAs. To investigate alterations in miRNA levels, we performed small RNA-seq on striatal brain tissue dissected 3 weeks after AAV-*wtHTT* and AAV-*mHTT* injections. This time point was chosen because there were no major cell death or phenotypic changes in the surrounding glia and only minor electrophysiological alterations in striatal neurons, representing an early time point in the disease course (Figures S2F–S2Q and S5C; Table S3). When investigating global miRNA levels, we found a more than 50% global increase in mature miRNA levels in AAV-*mHTT*-injected mice compared to AAV-*wtHTT*-injected mice (Figures 4A and 4B). We found that most individual miRNAs were overexpressed, including abundant neuronal miRNAs such as miR-128, miR-9, and let-7

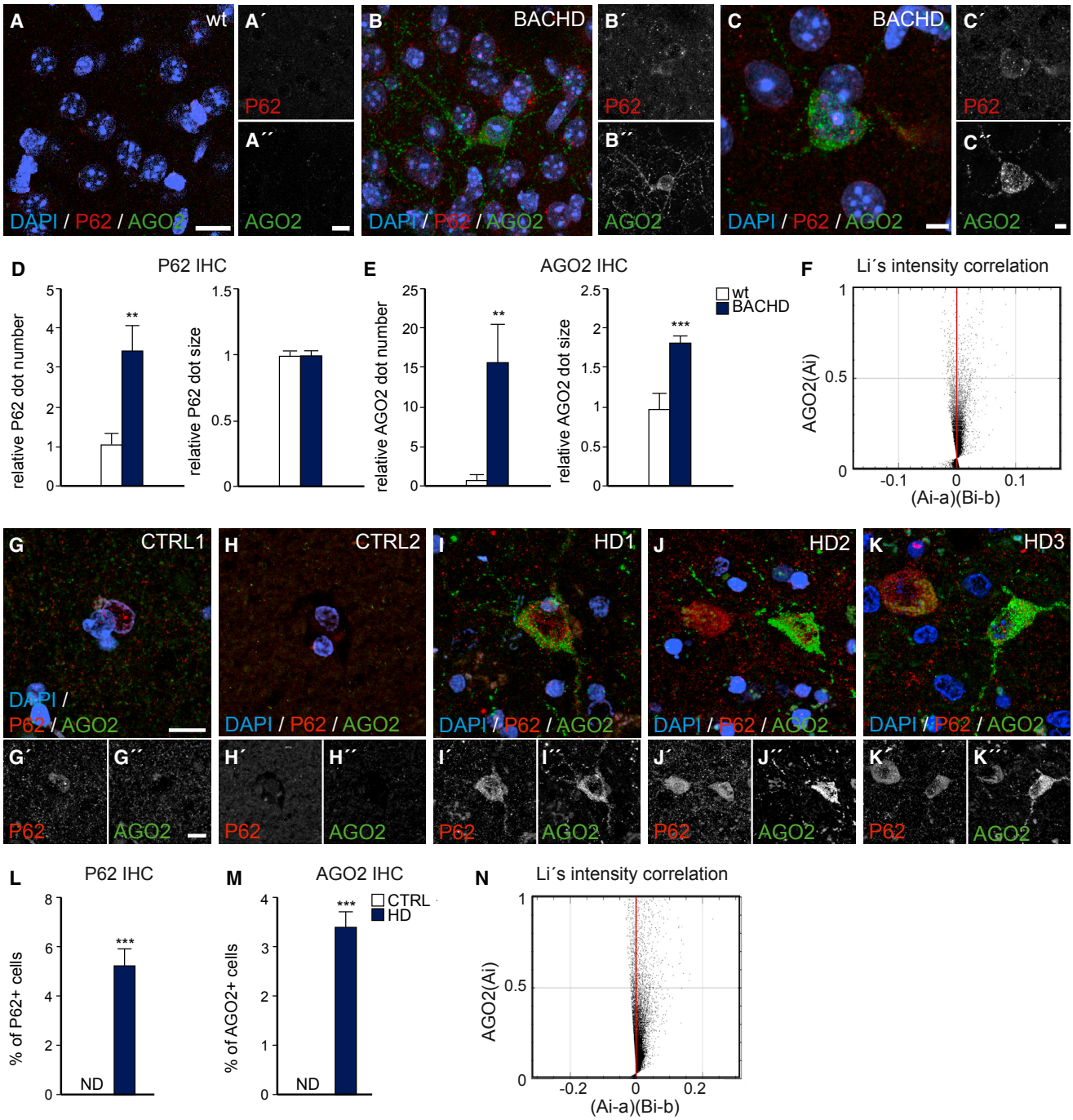

Figure 3. p62 and AGO2 Accumulate in BACHD Mice and in Post-mortem Material from HD Patients

(A–E) p62 (D) and AGO2 (E) accumulate in the striatal tissue of BACHD mice (B and C) but not in wt animals (A). n = 18 (3 animals/ group).

(F) Li's intensity correlation analysis shows that AGO2 and p62 have almost no colocalization, as indicated by the points mostly falling equally along the positive and negative sides of the x axis. Ai: AGO2 intensity; Bi: p62 intensity.

(G–M) There was a clear accumulation of AGO2 (M) and p62 (L) in all of the HD post-mortem tissue (I–K) but not in the healthy control tissue (G and H). (L) For p62 statistical analysis, 542 and 1,658 DAPI+ cells were analyzed in 2 control and 3 HD patients, respectively. (M) For AGO2 statistical analysis, 772 and 2,032 DAPI+ cells were analyzed in 2 control and 3 HD patients, respectively.

(N) AGO2 and p62 puncta accumulated inside neurons and did not colocalize. Ai: AGO2 intensity; Bi: p62 intensity.

ND: non-detectable; ***$p < 0.001$; **$p < 0.01$; two-tailed two-sample unequal variance t tests. All data are shown as mean ± SEM. Scale bars represent 25 μm (A and B), 5 μm (C), and 12.5 μm (G–K). See also Figure S5 and Tables S1 and S2.

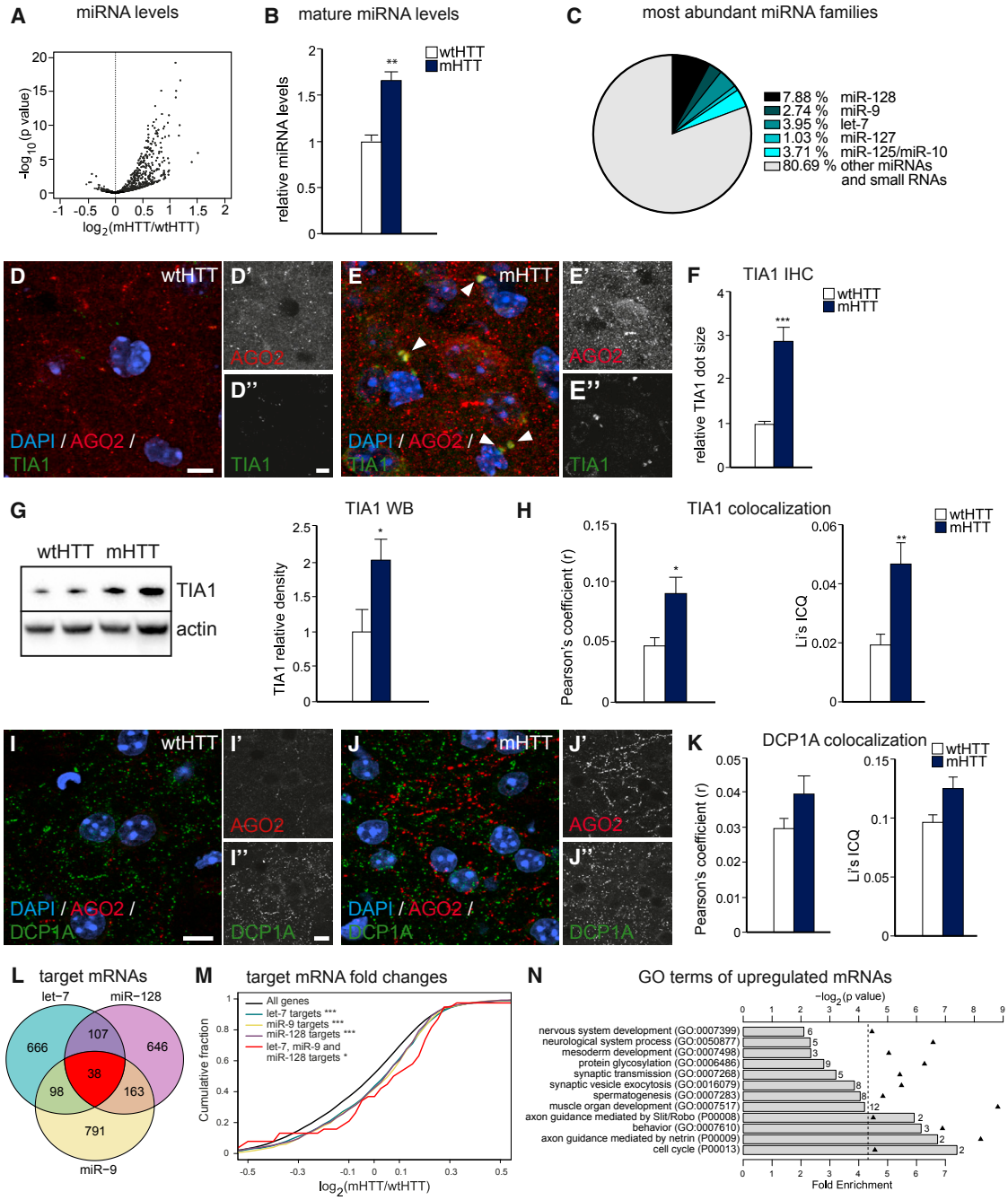

Figure 4. miRNAs and SGs Accumulate in Neurons Expressing Protein Aggregates

(A) Volcano plot summarizing the fold changes of all miRNAs after 3 weeks in AAV-*mHTT*-injected animals compared to AAV-*wtHTT*. n = 3 (8 animals/sample, Wald chi-square test).

(B) Levels of mature miRNAs are increased in AAV-*mHTT*-injected animals compared to AAV-*wtHTT*-injected controls 3 weeks after injection. n = 3 (8 animals/sample).

(C) Distribution of the most abundant miRNA families after 3 weeks of AAV-*wtHTT*-injected animals. n = 3 (8 animals/sample).

(D–F) TIA1 accumulated in AAV-*mHTT* (E)-injected animals compared to AAV-*wtHTT* (D). (F) Overexpression of mHTT significantly increased TIA1 size. n = 11 for AAV-*wtHTT* and n = 9 for AAV-*mHTT* (3 animals/group).

(G) TIA1 protein level was significantly higher in AAV-*mHTT*-injected animals compared to AAV-*wtHTT*. n = 10 or 8 (5 animals in the AAV-*wtHTT* group and 4 animals in the AAV-*mHTT*-injected group).

(H) TIA1 showed increased colocalization with AGO2. n = 11 for AAV-*wtHTT* and n = 9 for AAV-*mHTT* (3 animals/group).

(legend continued on next page)

(Figures 4C, S5D, and S5E). These data demonstrate that the increase in AGO2 levels correlates with an increased level of mature miRNAs.

AGO2 Puncta Localize to Stress Granules, Resulting in Loss of miRNA Activity

The subcellular localization of AGO2 is known to be important for the activity of miRNA-mediated gene silencing (Leung and Sharp, 2013). This suggests that alterations of AGO2 levels as well as accumulation of AGO2 in puncta in mHTT-expressing neurons may affect the activity of miRNAs. AGO2 protein is normally diffusely distributed throughout the cytoplasm but has also been found in processing bodies (P-bodies) and stress granules (SGs) (Anderson and Kedersha, 2006; Leung and Sharp, 2013). The shuffling of AGO2 through different cytoplasmic compartments is directly related to the activity of miRNAs. For example, AGO2 found in SGs contains miRNAs but does not participate in gene silencing (Leung and Sharp, 2013).

In mice injected with AAV-*mHTT*, we found a 4-fold increase in the size of SGs, as monitored with the cytotoxic granule-associated RNA binding protein TIA1 (Figures 4D–4F). We also found an increase in total TIA1 levels, as measured with WB (Figure 4G). Remarkably, we found a clear increase in the amount of AGO2 localizing to SGs in mHTT-expressing cells (Figures 4D, 4E, and 4H; Table S1). On the contrary, we did not find a significant increase in colocalization of AGO2 puncta to P-bodies (Figures 4I–4K; Table S1). We also found that overexpression of AAV-BECN1, together with AAV-mHTT, significantly reduced TIA1 colocalization with AGO2 (Figures S5F–S5H; Table S1). These data demonstrate that a substantial fraction of AGO2 re-localizes to SGs in mHTT-expressing neurons. Because AGO2-miRNA complexes lose their silencing activity in SGs, this indicates that an overall loss of miRNA activity should occur following mHTT expression.

To test this hypothesis, we investigated neuronal miRNA activity by performing RNA-seq on striatal tissue injected with either AAV-*mHTT* or AAV-*wtHTT* and quantified the expression of all detectable mRNAs. We then selected targets of three of the most highly expressed neuronal miRNAs in the mouse striatum, miR-128, let-7, and miR-9, based on computationally predicted and evolutionary conserved miRNA target sites (TargetScanMouse 7.1) (Figure 4L; Table S4; Agarwal et al., 2015). We assessed the global fold change distribution of targets in cumulative fraction graphs (y axis) and found that the expression levels of these miRNA targets, but not non-neuronal miRNA targets or non-targeted mRNAs, were significantly increased in AAV-*mHTT*-injected animals, indicating a de-repression of targets of the most abundant neuronal miRNAs (Figures 4M and S5I). Interestingly, genes targeted by all three miRNAs showed an even stronger shift toward de-repression (Figure 4M). Together, these results are in line with other studies where re-localization of AGO2 to SGs is associated with a loss of miRNA activity (Leung and Sharp, 2013; Qi et al., 2008; Wu et al., 2011).

To investigate the potential function of the de-repressed miRNA targets, we performed gene ontology analysis on the set of genes targeted by the three most abundant miRNAs (let-7, miR-128, and miR-9) and found these to be highly enriched for terms such as neurological system processes, axon guidance, and synaptic functions (Figures 4N and S5J). These are all mechanisms that are disrupted in HD and other NDDs. In an independent analysis, we also confirmed that experimentally identified neuronal miR-128 targets were upregulated upon mHTT expression (Figure S5K; Tan et al., 2013). It is worth noting that the phenotype of miR-128 KO mice is characterized by neuronal hyperactivity, a phenomenon that is also found in models of HD, directly linking our analysis to HD-like phenotypes (Tan et al., 2013).

DISCUSSION

Several hundred miRNAs are expressed in the brain and are thought to regulate thousands of transcripts (Petri et al., 2014). Therefore, any alteration in the miRNA network is likely to have a significant effect on neuronal function. In line with this, there is extensive literature documenting that conditional deletion of *Dicer* or individual miRNAs such as miR-128 in postmitotic neurons (including striatal neurons) results in phenotypes that are reminiscent of HD (Cheng et al., 2014; Schaefer et al., 2007; Tan et al., 2013). Thus, an alteration in miRNA activity in HD and other NDDs is likely to contribute to the early intracellular pathology, including alterations in neuronal activity and synaptic plasticity.

The current work provides mechanistic insight into how protein aggregation causes global alterations of miRNA level and activity through a direct link between impaired autophagy and AGO2 accumulation because of mHTT expression. Our results are in line with previous studies demonstrating that selective autophagy is required to maintain appropriate AGO2 levels and that AGO2 levels need to be carefully regulated to sustain appropriate levels of mature miRNAs (Füllgrabe et al., 2014; Gibbings et al., 2012; He et al., 2012; Savas et al., 2008). However, a previous study

(I–K) There was no difference in the level of AGO2 co-staining with DCP1A between AAV-*wtHTT* (I) and *mHTT* (J)-injected animals. (K) Overexpression of mHTT did not change DCP1A and AGO2 colocalization. n = 6 (3 animals/group).

(L) Venn diagram showing the number of unique and shared target genes of let-7, miR-9, and miR-128, as predicted by TargetScan. Only genes with more than 16 reads on average were included and used in the downstream miRNA target analysis. n = 3 (1 animal/ RNA sample).

(M) Cumulative fractions of $\log_2$(mHTT/wtHTT) fold changes of expressed genes (>16 reads) and the predicted targets of let-7, miR-9, and miR-128 as well as the 38 shared targets show a significant upregulation in AAV-*mHTT* compared to AAV-*wtHTT*-injected animals. n = 3 (1 animal/sample). *p < 0.05, ***p < 0.001; Wilcoxon rank-sum test with continuity correction was applied to target genes versus all genes).

(N) The top 12 most enriched Panther gene ontologies among the set of significantly upregulated ($\log_2$ fold-change > 0.1; *p < 0.05, n = 183) let-7, miR-9, and miR-128 target genes. Fold enrichment: observed number of genes/expected from background population of all expressed genes (>16 reads). Black triangles: p value, binomial distribution test. Numbers by bars indicate the number of observed genes for the given term.

All fold changes are shown as $\log_2$(mHTT/wtHTT). WB values were normalized to AAV-*wtHTT*-injected expression levels and corrected to actin values. ***p < 0.001; **p < 0.01; *p < 0.05; two-tailed two-sample unequal variance t tests. All data are shown as mean ± SEM. Scale bars represent 5 μm (D and E) and 7.5 μm (I and J). See also Figure S5 and Tables S1, S2, S4, S5, and S6.

performed in cancer cell lines found that AGO2 accumulation because of impaired autophagy results in a loss of mature miRNAs. In this study, the authors speculated that this phenomenon was due to an imbalance in the stoichiometry of the RISC complex components (Gibbings et al., 2012). When we analyzed 293T cells expressing mHTT, we found similar results, including global loss of mature miRNAs (Figures S5L and S5M). However, mature neurons do not divide, and, thus, any impairments in autophagy are likely to have different consequences than in dividing cells, which can renew their cytoplasmic content upon cell division.

We found that accumulation of AGO2 in neurons expressing mHTT is linked to accumulation of mature miRNAs. However, mHTT expression also causes a shift in AGO2 localization to SGs, resulting in global loss of miRNA activity despite the increase in mature miRNAs. It thus appears that the consequence of AGO2 accumulation is fundamentally different between neurons and dividing cells, which could be due to the inability of neurons to renew their protein composition during cell division or through the appearance of SGs in mHTT-expressing neurons.

In this study, we used an AAV-based *in vivo* mouse model. This model has several advantages for studying the transcriptional response to mHTT because it allows for an appropriate control (AAV-*wtHTT*) and results in neuron-specific expression of mHTT, limiting the effect on surrounding glial cells that otherwise may complicate the analysis. Compared to most transgenic mouse models of NDDs, it also avoids potential developmental or compensatory effects that might arise because of transgene expression in the entire organism during brain development. Our data show that alterations in AGO2 levels following mHTT expression occur at an early time point during the disease course. AGO2 and mature miRNAs are already accumulating 3 weeks following AAV-*mHTT* injection, a time point when only minor alterations in neuronal functions can be detected, as monitored by DARPP-32 levels or electrophysiological recordings. This suggests that loss of miRNA activity may be an important component of early disease phenotypes in HD. In this respect, our data are in line with a previous study that found a global accumulation of miRNAs at an early stage in a mouse model of HD, and there are also data indicating that mHTT expression impairs miRNA silencing in cell lines (Lee et al., 2011; Savas et al., 2008). In contrast, our results are inconsistent with several reports of either selective up- or downregulation of individual miRNAs or reports of a global loss of miRNAs in more severe HD mouse models or when analyzing post-mortem tissue (Kocerha et al., 2014; Maciotta et al., 2013). This discrepancy may, to some extent, be explained by differences in methodology as well as some limitations when using various mouse models and post-mortem material. Alternatively, it may also result from the fact that impairments of the miRNA machinery change as the disease progresses. When we analyzed striatal tissue 6 months after AAV-*mHTT* injection, when there was clear evidence of striatal and ventricle volume changes that was coupled with atrophy and gliosis, thus reflecting a later-stage time point, we rather find a decrease in AGO2 protein level, as measured by WB, and only detected sparse neurons displaying AGO2 accumulation (Figures S6A–S6Y). Similar, we found lower AGO2 levels from HD post-mortem striatal tissue when analyzing global protein levels using WB (Figure S6Z). These data raise the possibility that AGO2 accumulation accompanied by a loss of miRNA activity is a specific feature of early-stage impairment in neurons expressing protein aggregates and impaired autophagy.

In summary, our results suggest that changes in miRNA levels are an early feature of HD that lies downstream of alterations in autophagy. Our data provide a mechanistic link between protein aggregation and post-transcriptional gene regulation, two seemingly unrelated phenomena. Our data also provide further support for developing autophagy-activating therapeutic approaches for HD and other NDDs because they suggest that activation of autophagy will not only clear toxic protein aggregates but also directly restore dysfunctional post-transcriptional gene regulation.

EXPERIMENTAL PROCEDURES

Detailed experimental procedures can be found in the Supplemental Experimental Procedures.

Viral Vectors

To overexpress wtHTT and mHTT, we used previously described third-generation self-inactivating lentiviral vectors encoding the first 171 amino acids of the human huntingtin gene with 18 or 66 CAG repeats under the control of a mouse phosphoglycerate kinase 1 promoter (PGK) (de Almeida et al., 2002).

Animal Surgery

All animal-related procedures were approved and conducted in accordance with the Committee for Use of Laboratory Animals at Lund University. All mice were adult C57BL/6 females 9 to 10 weeks old at the time of surgery. All stereotactic injections into the striatum were performed as described before with minor changes (Petri et al., 2017). Injections were unilateral on the right side of the brain with a total of 1 μl of injected virus. The injection coordinates were as follows: anterior/posterior (AP): +0.9 mm; medial/lateral (ML): +/−1.8 mm; dorsal/ventral (DV) (from the dura): −2.7 mm.

Human Tissue

Post-mortem human brain tissue was obtained from the Cambridge Brain Bank (Cambridge, UK) and used under local ethics approval (REC 01/177).

Small RNA-Seq

cDNA libraries of small RNA-seq samples were prepared using the New England Biolabs Small RNA Library Prep Kit for small RNA-seq at the Clinical Microarray Core (University of California, Los Angeles [UCLA], CA, USA). Illumina high-throughput sequencing was applied to the samples (total number of reads: *in vivo*, 228,894,902; *in vitro*, 71,800,132).

RNA-Seq

cDNA libraries of the *in vitro* mRNA samples were prepared using the KAPA Stranded mRNA-Seq Kit from KAPAbiosystems at the Clinical Microarray Core (UCLA, CA, USA). *In vivo* cDNA libraries were prepared using the Illumina Strand-Specific TruSeq RNA Library Kit using poly(A) selection and sent for sequencing to SciLifeLab. Illumina high-throughput sequencing was applied to all the samples (total read number: *in vitro*, 180,491,336; *in vivo*, 356,983,073).

Statistical Analysis

Two-tailed, two-sample unequal variance t tests were used to analyze means in most cases. One-way ANOVA or nonparametric Kruskal-Wallis test was used in Figures 1B, S1B–S1D, S1M, and S1N with Figures S1Q and S1S depending on normal distribution defined by D'Agostino-Pearson omnibus normality test. The criterion for significance for all analyses was $p < 0.05$. All data are shown as mean ± SEM.

DATA AND SOFTWARE AVAILABILITY

The accession number for the RNA-seq and small RNA-seq data reported in this paper is GEO: GSE78928.

SUPPLEMENTAL INFORMATION

Supplemental Information includes Supplemental Experimental Procedures, six figures, and six tables and can be found with this article online at https://doi.org/10.1016/j.celrep.2018.07.017.

ACKNOWLEDGMENTS

We are grateful to all members of the Jakobsson lab as well as Bengt Mattsson and Janelle Drouin-Ouellet for stimulating discussions and useful comments on the manuscript. We also thank U. Jarl, J. Johansson, M. Persson Vejgården, I. Nilsson, E. Ling, M. Sparrenius, U. Samuelsson, A. Josefsson, and A. Hammarberg for technical assistance. We thank the Cambridge Brain Bank for the post-mortem tissue and the support it receives from the NIHR award of a Biomedical Research Centre to Addenbrooke's Hospital and the University of Cambridge. This work was supported by grants from the Swedish Research Council (K2014-62X-22527-01-3 and K2014-62X-20404-08-5), the Swedish Foundation for Strategic Research (FFL12-0074), the Swedish Brain Foundation (FO2014-0106), the Swedish Excellence Project Basal Ganglia Disorders Linnaeus Consortium (Bagadilico), and the Swedish Government Initiative for Strategic Research Areas (MultiPark and StemTherapy).

AUTHOR CONTRIBUTIONS

K.P., R.P., S.M., P.L.B., R.V., D.R.O., I.S.-A., B.A.H., M.M.-B., S.H.L., Å.P., N.D., S.S.H., M.P., R.A.B., and J.J. designed and performed the research and analyzed data. R.P., P.L.B., and M.M.-B. performed the bioinformatics analysis. K.P. and J.J. designed and coordinated the project and analyzed data. K.P. and J.J. wrote the paper, and all authors reviewed the manuscript.

DECLARATION OF INTERESTS

The authors declare no competing interests.

Received: November 3, 2017
Revised: April 19, 2018
Accepted: July 4, 2018
Published: August 7, 2018

REFERENCES

Agarwal, V., Bell, G.W., Nam, J.W., and Bartel, D.P. (2015). Predicting effective microRNA target sites in mammalian mRNAs. eLife *4*.

Anderson, P., and Kedersha, N. (2006). RNA granules. J. Cell Biol. *172*, 803–808.

Bossé, G.D., and Simard, M.J. (2010). A new twist in the microRNA pathway: Not Dicer but Argonaute is required for a microRNA production. Cell Res. *20*, 735–737.

Cheng, S., Zhang, C., Xu, C., Wang, L., Zou, X., and Chen, G. (2014). Age-dependent neuron loss is associated with impaired adult neurogenesis in forebrain neuron-specific Dicer conditional knockout mice. Int. J. Biochem. Cell Biol. *57*, 186–196.

Cortes, C.J., and La Spada, A.R. (2014). The many faces of autophagy dysfunction in Huntington's disease: from mechanism to therapy. Drug Discov. Today *19*, 963–971.

de Almeida, L.P., Ross, C.A., Zala, D., Aebischer, P., and Déglon, N. (2002). Lentiviral-mediated delivery of mutant huntingtin in the striatum of rats induces a selective neuropathology modulated by polyglutamine repeat size, huntingtin expression levels, and protein length. J. Neurosci. *22*, 3473–3483.

Diederichs, S., and Haber, D.A. (2007). Dual role for argonautes in microRNA processing and posttranscriptional regulation of microRNA expression. Cell *131*, 1097–1108.

DiFiglia, M., Sapp, E., Chase, K.O., Davies, S.W., Bates, G.P., Vonsattel, J.P., and Aronin, N. (1997). Aggregation of huntingtin in neuronal intranuclear inclusions and dystrophic neurites in brain. Science *277*, 1990–1993.

Füllgrabe, J., Klionsky, D.J., and Joseph, B. (2014). The return of the nucleus: transcriptional and epigenetic control of autophagy. Nat. Rev. Mol. Cell Biol. *15*, 65–74.

Gibbings, D., Mostowy, S., Jay, F., Schwab, Y., Cossart, P., and Voinnet, O. (2012). Selective autophagy degrades DICER and AGO2 and regulates miRNA activity. Nat. Cell Biol. *14*, 1314–1321.

Gray, M., Shirasaki, D.I., Cepeda, C., André, V.M., Wilburn, B., Lu, X.H., Tao, J., Yamazaki, I., Li, S.H., Sun, Y.E., et al. (2008). Full-length human mutant huntingtin with a stable polyglutamine repeat can elicit progressive and selective neuropathogenesis in BACHD mice. J. Neurosci. *28*, 6182–6195.

He, M., Liu, Y., Wang, X., Zhang, M.Q., Hannon, G.J., and Huang, Z.J. (2012). Cell-type-based analysis of microRNA profiles in the mouse brain. Neuron *73*, 35–48.

Kocerha, J., Xu, Y., Prucha, M.S., Zhao, D., and Chan, A.W. (2014). microRNA-128a dysregulation in transgenic Huntington's disease monkeys. Mol. Brain *7*, 46.

Lee, S.T., Chu, K., Im, W.S., Yoon, H.J., Im, J.Y., Park, J.E., Park, K.H., Jung, K.H., Lee, S.K., Kim, M., and Roh, J.K. (2011). Altered microRNA regulation in Huntington's disease models. Exp. Neurol. *227*, 172–179.

Leung, A.K., and Sharp, P.A. (2013). Quantifying Argonaute proteins in and out of GW/P-bodies: implications in microRNA activities. Adv. Exp. Med. Biol. *768*, 165–182.

Maciotta, S., Meregalli, M., and Torrente, Y. (2013). The involvement of microRNAs in neurodegenerative diseases. Front. Cell. Neurosci. *7*, 265.

Martin, D.D., Ladha, S., Ehrnhoefer, D.E., and Hayden, M.R. (2015). Autophagy in Huntington disease and huntingtin in autophagy. Trends Neurosci. *38*, 26–35.

Pang, X., Hogan, E.M., Casserly, A., Gao, G., Gardner, P.D., and Tapper, A.R. (2014). Dicer expression is essential for adult midbrain dopaminergic neuron maintenance and survival. Mol. Cell. Neurosci. *58*, 22–28.

Petri, R., Malmevik, J., Fasching, L., Åkerblom, M., and Jakobsson, J. (2014). miRNAs in brain development. Exp. Cell Res. *321*, 84–89.

Petri, R., Pircs, K., Jönsson, M.E., Åkerblom, M., Brattås, P.L., Klussendorf, T., and Jakobsson, J. (2017). let-7 regulates radial migration of new-born neurons through positive regulation of autophagy. EMBO J. *36*, 1379–1391.

Qi, H.H., Ongusaha, P.P., Myllyharju, J., Cheng, D., Pakkanen, O., Shi, Y., Lee, S.W., Peng, J., and Shi, Y. (2008). Prolyl 4-hydroxylation regulates Argonaute 2 stability. Nature *455*, 421–424.

Savas, J.N., Makusky, A., Ottosen, S., Baillat, D., Then, F., Krainc, D., Shiekhattar, R., Markey, S.P., and Tanese, N. (2008). Huntington's disease protein contributes to RNA-mediated gene silencing through association with Argonaute and P bodies. Proc. Natl. Acad. Sci. USA *105*, 10820–10825.

Schaefer, A., O'Carroll, D., Tan, C.L., Hillman, D., Sugimori, M., Llinas, R., and Greengard, P. (2007). Cerebellar neurodegeneration in the absence of microRNAs. J. Exp. Med. *204*, 1553–1558.

Tan, C.L., Plotkin, J.L., Venø, M.T., von Schimmelmann, M., Feinberg, P., Mann, S., Handler, A., Kjems, J., Surmeier, D.J., O'Carroll, D., et al. (2013). MicroRNA-128 governs neuronal excitability and motor behavior in mice. Science *342*, 1254–1258.

Wu, C., So, J., Davis-Dusenbery, B.N., Qi, H.H., Bloch, D.B., Shi, Y., Lagna, G., and Hata, A. (2011). Hypoxia potentiates microRNA-mediated gene silencing through posttranslational modification of Argonaute2. Mol. Cell. Biol. *31*, 4760–4774.

Yamamoto, A., and Yue, Z. (2014). Autophagy and its normal and pathogenic states in the brain. Annu. Rev. Neurosci. *37*, 55–78.

Cell Reports, Volume *24*

Supplemental Information

Huntingtin Aggregation Impairs Autophagy, Leading to Argonaute-2 Accumulation and Global MicroRNA Dysregulation

Karolina Pircs, Rebecca Petri, Sofia Madsen, Per Ludvik Brattås, Romina Vuono, Daniella R. Ottosson, Isabelle St-Amour, Bob A. Hersbach, Monika Matusiak-Brückner, Sofia Hult Lundh, Åsa Petersén, Nicole Déglon, Sébastien S. Hébert, Malin Parmar, Roger A. Barker, and Johan Jakobsson

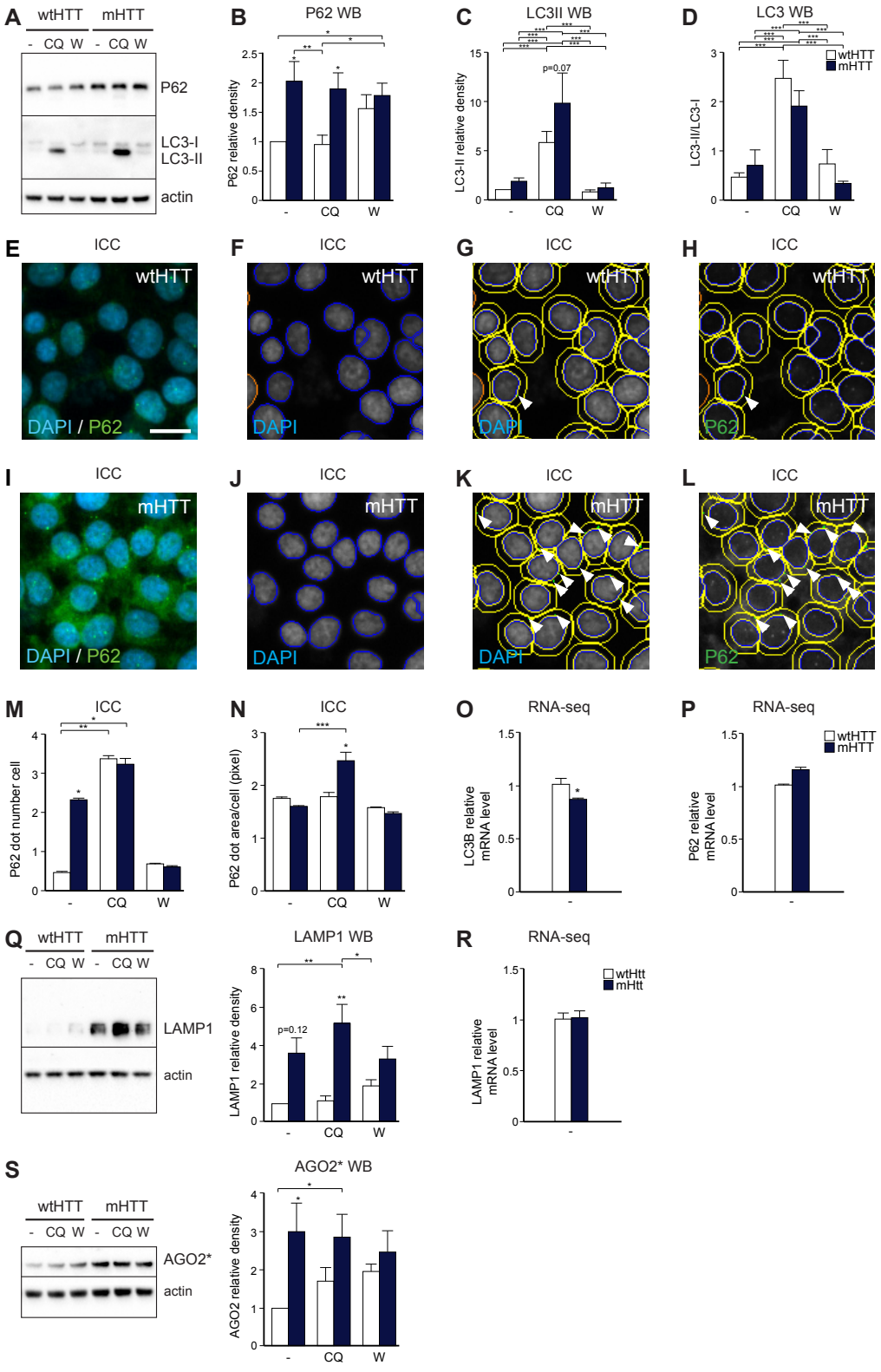

Figure S1. mHTT expression alters autophagy and results in accumulation of AGO2 *in vitro*. Related to Figure 1.

(A-D) WB autophagic protein expression level in LV-*mHTT* and LV-*HTT* transduced cells (A). p62 (B) and LC3 (C) accumulated in the non-treated and CQ treated, but not in the W

treated mHTT expressing cells, which indicates that mHTT-expression leads to impaired basal autophagy. LC3-II/LC3-I ratio (D) was reduced after CQ treatment in mHTT expressing cells but not after the other treatments. n = 8/ each condition.

(E-L) ICC pictures taken from high-content screening (HSC) measurements of LV-wtHTT (E) and mHTT (I) expressing cells. The program defines the cells based on DAPI staining (F and J) and defines the cytoplasm as a ring around the nuclei (G and K). p62 dots detected within the ring are quantified for each cell (H and L). Arrowheads show p62 aggregates marked with green.

(M-N) There were significantly more p62 dots in the non-treated mHTT overexpressing cells measured by HSC (M). p62 aggregated in the mHTT, but not in the wtHTT expressing cells after CQ treatment (N). There was no difference in p62 size or number after W treatment in wtHTT and mHTT expressing cells (N). n = 6/ each condition.

(O-P) No major changes at the mRNA level was measured in the non-treated LV-wtHTT or mHTT overexpressing cells for p62 (P) or LC3 (O). n = 3 (1 animal/ RNA sample).

(Q) LAMP1 accumulated in the mHTT but not in the wtHTT overexpressing cells. n = 4/ each condition.

(R) No major changes at the mRNA level was measured in the non-treated LV-wtHTT or mHTT overexpressing cells for LAMP1. n = 3 (1 animal/ RNA sample).

(S) There was an elevated expression of AGO2 protein in the mHTT expressing cells using AGO2* antibody. AGO2 protein levels increased after autophagic impairment induced by CQ or W in the LV-wtHTT overexpressing cells. n = 4/ each condition.

WB values were normalized to LV-*wtHTT* non-treated expression levels and corrected to actin values. ***$p<0.001$; **$p<0.001$; *$p<0.05$; One-way ANOVA (C, D, M, Q) or nonparametric Kruskal-Wallis test (B, N, S) was used depending on normal distribution defined by D'Agostino-Pearson omnibus normality test. Two-tailed two-sample unequal variance t-tests was used for O, P and R. All data are shown as mean ± SEM. Scale bars represent 10 μm (E-L).

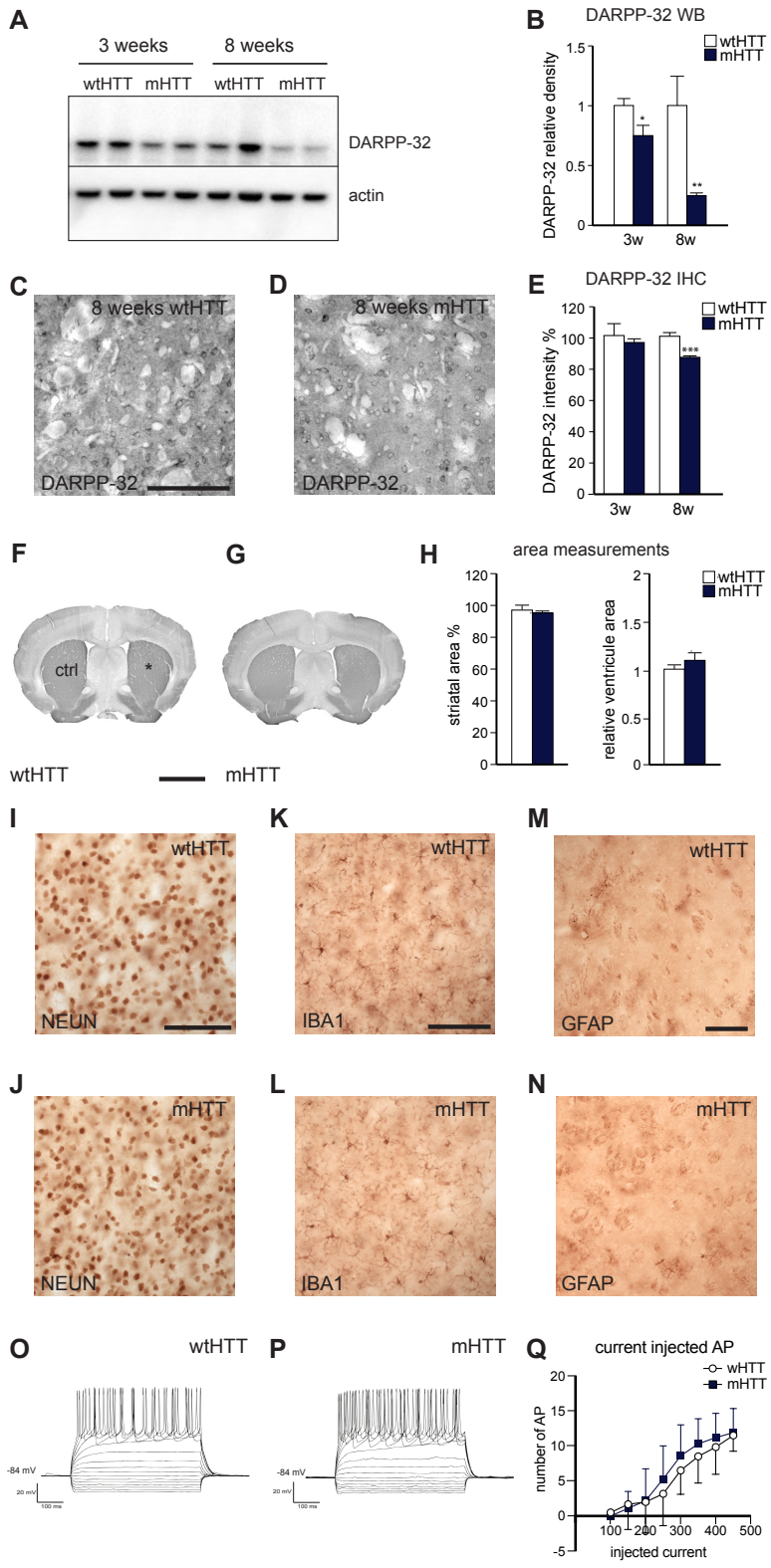

Figure S2. Characterization of a progressive AAV-based mouse model of HD. Related to Figure 1.

(A-B) WB DARPP-32 expression level in AAV-*mHTT* and *wtHTT* injected animals (A). Gradual decrease of DARPP-32 protein was detected in AAV-*mHTT* animals at 3 and 8

weeks after injection (B). n = 8 (4 animals/ group).

(C-E) IHC demonstrate less DARPP-32 expression in the AAV-*mHTT* (D) compared to AAV-*wtHTT* (C) injected animals. Densitometrical analysis revealed a significant loss of DARPP-32 protein after 8 weeks of AAV-*mHTT* injection (E). n = 12 (4 animals/ group).

(F-H) Striatal and ventricle area measurements showed no difference between the AAV-*wtHTT* (F) and AAV-*mHTT* (G) injected animals after 8 weeks (H). The injected side is marked with an asterisk. n = 12 (4 animals/ group).

(I-J) NeuN staining in the AAV-*mHTT* (J) and AAV-*wtHTT* (I) injected animals after 8 weeks.

(K-N) IBA1 and GFAP staining show no activated microglia or reactive astrocytes after 8 weeks in the AAV-*mHTT* (M and N) or AAV-*wtHTT* (K and L) injected animals.

(O-Q) Current-induced action potentials (AP) show no major difference between AAV-*mHTT* (O) and *wtHTT* (P) injected animals in the firing probability. Nevertheless, there is a small trend of slightly more firing for *mHTT*-injected animals (Q).

WB values are normalized to AAV-*wtHTT* expression levels and corrected to actin values. ***p<0.001; **p<0.001; *p<0.05; two-tailed two-sample unequal variance t-tests. All data are shown as mean ± SEM. Scale bars represent 50 μm (C and D), 50 μm (I-N), and 1.5 mm (F and G).

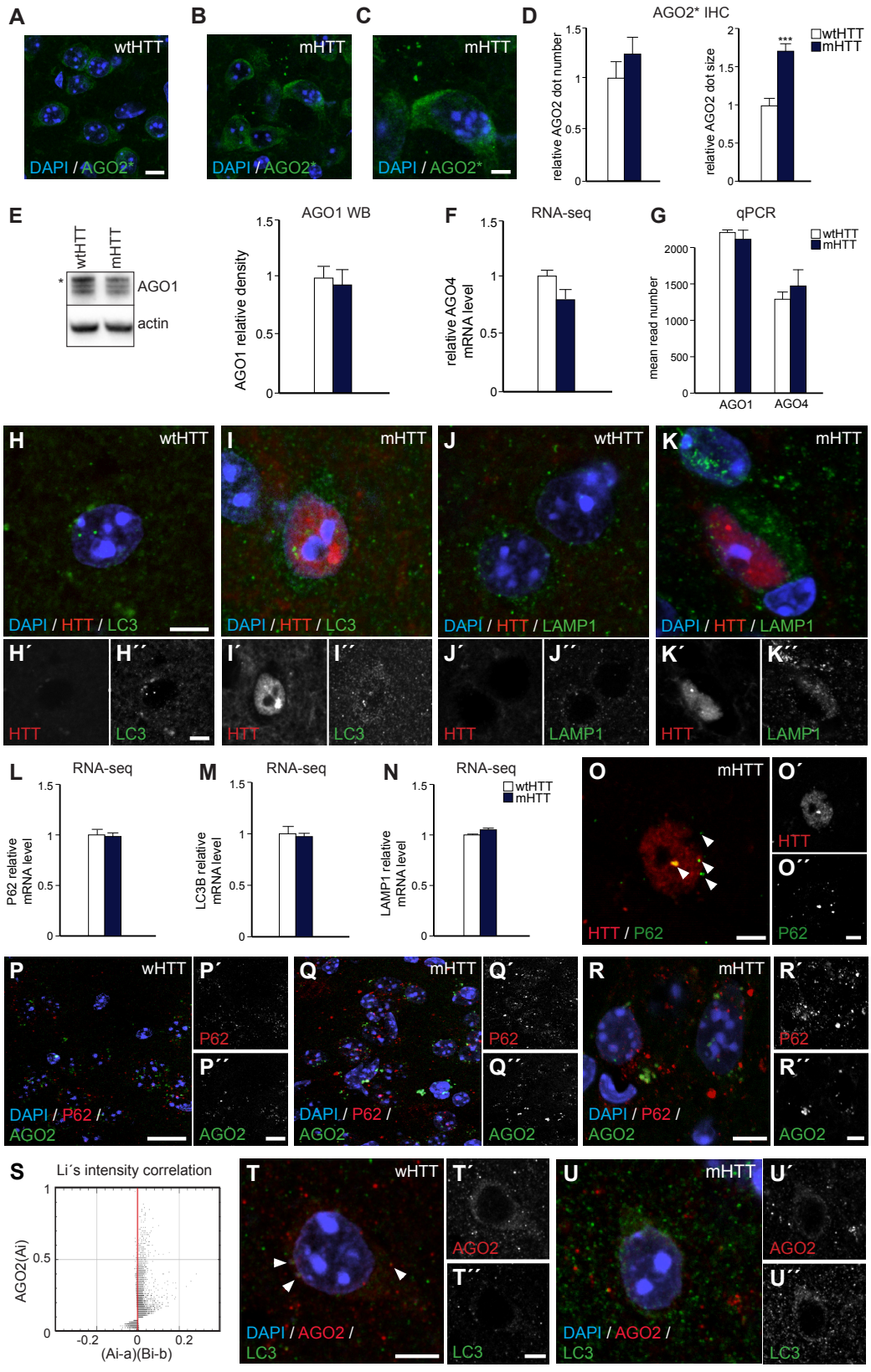

Figure S3. mHTT expression alters autophagy and results in accumulation of AGO2 *in vivo*. Related to Figure 1.

(A-D) AGO2* protein accumulates in the AAV-*mHTT* (B and C) but not in the AAV-

wtHTT (A) injected animals 8 weeks after injection. There were significantly bigger puncta in the AAV-*mHTT* injected mice than in those injected with AAV-*wtHTT* (D). n = 24 for AAV-*wtHTT*, and 27 for AAV-*mHTT* (3 animals/ group).

(E) AGO1 WB does not show any difference after 3 weeks of AAV-*wtHTT* or AAV-*mHTT* injection. AGO1 protein is marked with an asterisk. n = 10 (5 animals/ group).

(F) Relative AGO4 mRNA levels were not changed 3 weeks after AAV-mHTT overexpression with qPCR. n = 10 (5 animals/ group).

(G) RNA-seq experiments showed that AGO1 and AGO4 mRNA levels were not changed 3 weeks after AAV-mHTT overexpression. n = 3 (1 animal/ RNA sample).

(H-K) LC3 (I) and LAMP1 (K) accumulated around the HTT aggregates 3 weeks after AAV-*mHTT* injection compared to the *wtHTT* (H and J).

(L-N) There was no change at the mRNA level after 3 weeks for any of the used autophagic markers seen in Figure 1 P-T (p62 (L), LC3 (M), LAMP1 (N)). n = 3 (1 animal/ RNA sample).

(O) Arrowheads show p62 accumulation both inside and outside the outer surface of the HTT aggregates.

(P-R) p62 and AGO2 protein accumulated in the AAV-*mHTT* (Q and R) injected animals but not in the *wtHTT* animals (P).

(S) p62 and AGO2 did not show any clear colocalization visualized by Li's intensity correlation analysis. Ai: AGO2 intensity; Bi: p62 intensity.

(T-U) AGO2 colocalizes with autophagosomal marker LC3 in some cases in the AAV-*wtHTT* (T) but not in the AAV-*mHTT* (U) animals after 8 weeks of injection. Arrowheads highlighting the colocalizing puncta.

WB values are normalized to AAV-*wtHTT* expression levels and corrected to actin values. ***$p<0.001$; two-tailed two-sample unequal variance t-tests. All data are shown as mean ± SEM. Scale bars represent 7.5 μm (A and B), 3.75 μm (C), 2.5 μm (H-K, O, and R), 10 μm (P and Q), and 10 μm (T and U).

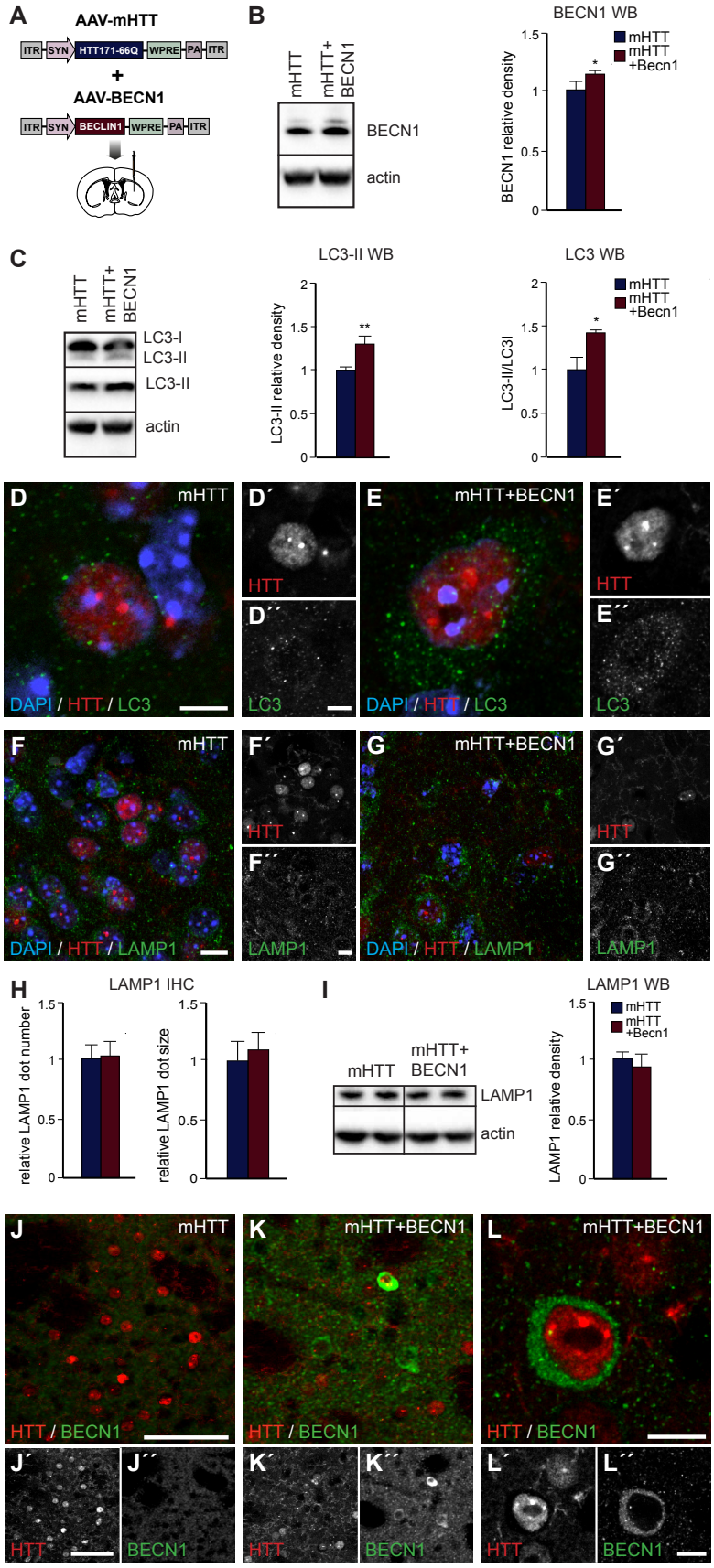

Figure S4. AAV-mediated delivery of Beclin1 reverses mHTT-associated phenotypes. Related to Figure 2.

(A) Experimental workflow summarizing the co-delivery of AAV-*mHTT* and AAV-*BECN1*.

(B) BECN1 protein level was significantly higher in the AAV-*BECN1* co-injected animals compared to AAV-*mHTT* injected animals. n = 4 (4 animals/ group).

(C) LC3-II protein level was significantly higher coupled with an increased LC3-II/LC3-I ratio in the AAV-*BECN1* co-injected animals compared to AAV-*mHTT* injected animals. n = 8 (4 animals/ group).

(D-E) LC3 dots accumulate inside and around the HTT aggregates 3 weeks after AAV-*mHTT*+*BECN1* co-injection (E) but not in the AAV-*mHTT* animals (D).

(F-H) LAMP1 dots did not accumulate inside and around the HTT aggregates 3 weeks after AAV-*mHTT*+*BECN1* co-injection (G) or AAV-*mHTT* injection (F). There was no difference in the relative LAMP1 dot number and size between the two groups (H). n = 26 (3 animals/ group).

(I) LAMP1 protein level did not change after AAV-*BECN1* co-injection compared to AAV-*mHTT* injected animals. n = 8 (4 animals/ group).

(J-K) Co-expression of BECN1 reduced the number of HTT aggregates (K) 3 weeks post injection compared to the AAV-*mHTT* injected animals (J).

(L) BECN1 surrounds the HTT aggregates.

WB values are normalized to AAV-*mHTT* expression levels and corrected to actin values. **p<0.01; *p<0.05; two-tailed two-sample unequal variance t-tests. All data are shown as mean ± SEM. Scale bars represent 2.5 μm (D, E and L) and 37.5 μm (F, G, J and K).

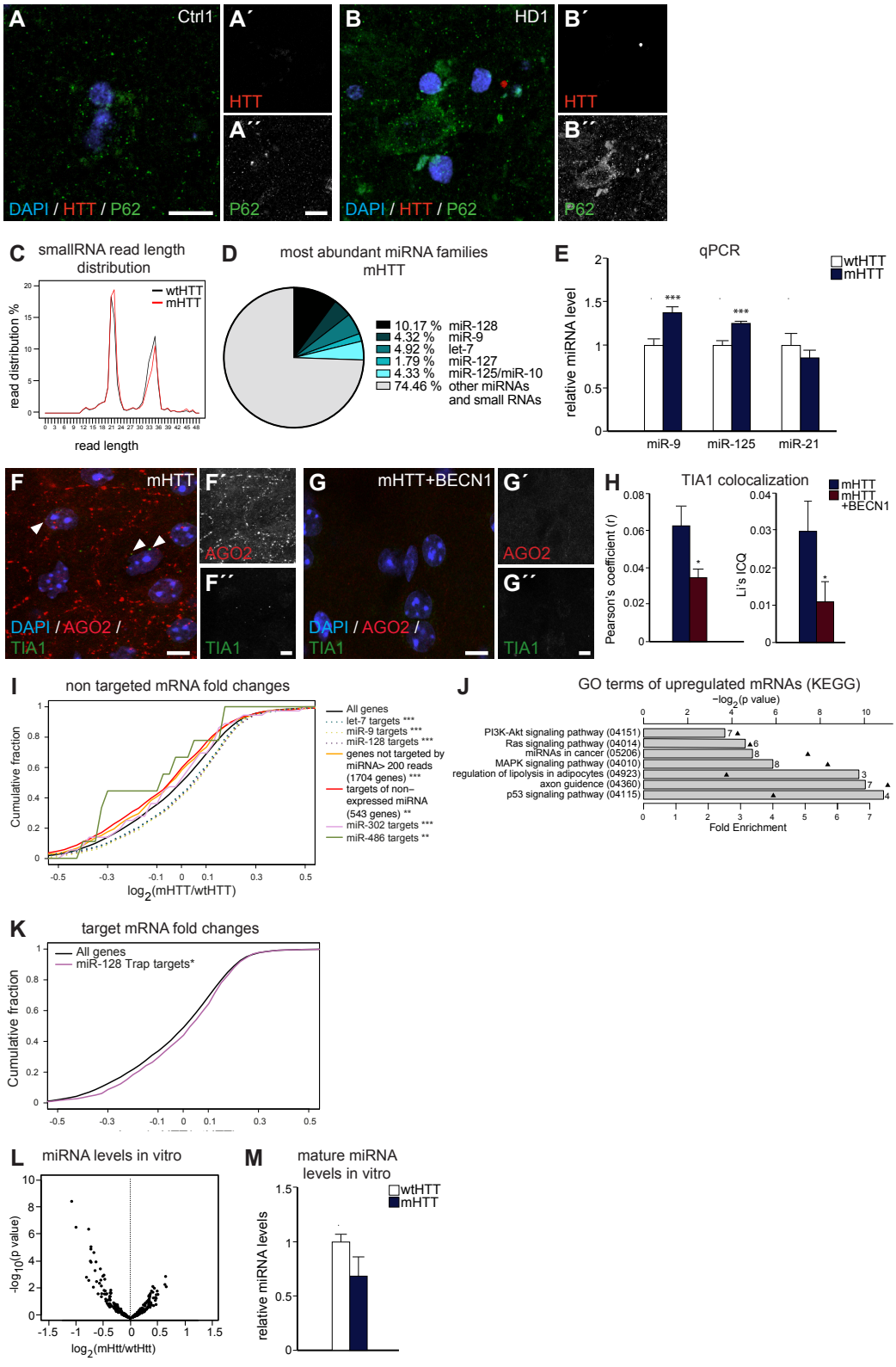

Figure S5. Related to Figure 3 and 4.

(A-B) p62 accumulates close to HTT aggregates in neurons of HD (B) patients but not in controls (A).

(C) Read distribution of small RNA-seq data obtained from AAV-*mHTT* or AAV-*wtHTT*

injected animals 3 weeks post-injection. n = 3 (8 animals/ small RNA sample).

(D) Distribution of the most abundant miRNA families after 3 weeks of AAV-*mHTT* injected animals. n = 3 (8 animals/ small RNA sample).

(E) qRT-PCR experiments showed significantly more neuronal miR-9 and miR-125 but not glial miR-21 relative miRNA expression level. n = 10 (5 animals/ group).

(F-H) TIA1 showed significantly decreased colocalization with AGO2 (H) in the co-injected animals (G) compared to the AAV-*mHTT* injected animals (F). n = 9 for AAV-*mHTT*, and AAV-*mHTT+Becn1* (3 animals/ group). *p<0.05; two-tailed two-sample unequal variance t-tests.

(I) Cumulative fractions of $\log_2$(mHTT/wtHTT) fold changes of expressed genes (>16 reads) and the predicted targets of highly expressed miRNAs (let-7, miR-9 and miR-128), non-expressed miRNAs (miR-302 and miR-486), as well as genes not targeted by any highly expressed miRNA. Let-7, miR-9 and miR-128 targets show a significant upregulation while miR-302 and miR-486 targets, as well as all genes not targeted by any highly expressed miRNA show a significant downregulation in AAV-*mHTT* compared to AAV-*wtHTT* injected animals. n = 3 (1 animal/ sample). *p<0.05; ***p-value<0.001; Wilcoxon rank sum test with continuity correction were applied on target genes versus all genes.

(J) Top 7 KEGG pathways among the set of significantly upregulated ($\log_2$ fold-change > 0.1; *p<0.05, n = 183) let-7, miR-9 and miR-128 target genes. Fold enrichment: Observed number of genes/expected from background population of all expressed genes (>16 reads). Black triangles: p-value, binomial distribution test. Numbers by bars indicate the number of observed genes for the given term.

(K) Cumulative fractions of $\log_2$(mHTT/wtHTT) fold changes of all expressed genes (>16 reads) and the expressed predicted targets of miR-128 (n = 1020).

(L) Volcano plot summarizing the fold changes of all miRNAs in the LV-*mHTT* transduced cells compared to the controls. n = 3.

(M) Levels of mature miRNAs are decreased in the LV-*mHTT* transduced cells compared to LV-*wtHTT*. n = 3.

***p<0.001; *p<0.05; two-tailed two-sample unequal variance t-tests. All data are shown as mean ± SEM. All fold changes are shown as $\log_2$(mHTT/wtHTT). Scale bars represent 25 μm (A and B), and 5 μm (F and G).

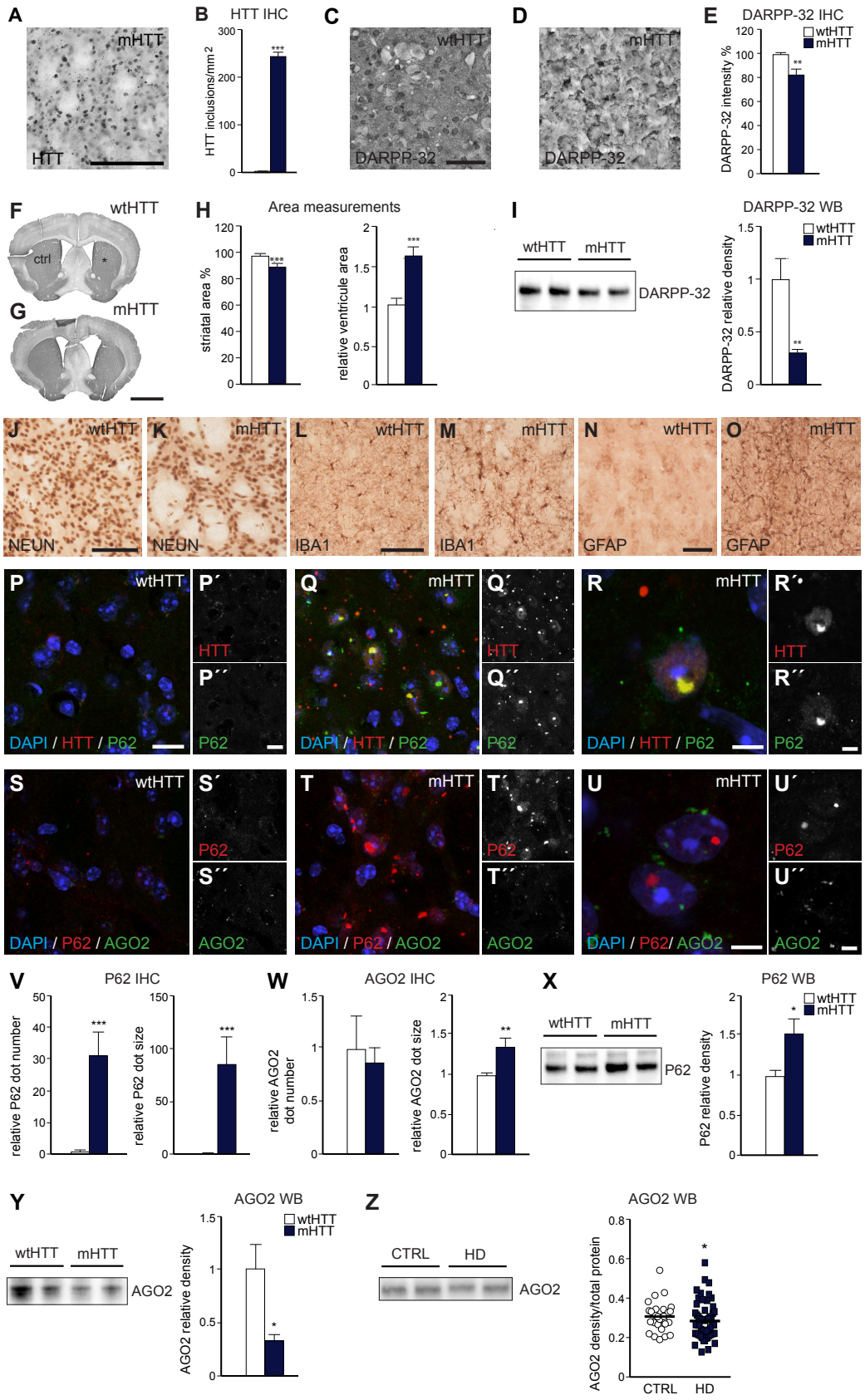

Figure S6. Characterization of a progressive AAV-based mouse model of HD after 6 months of injection. Related to Figure 1.

(A-B) HTT aggregates/mm^2 were present in AAV-*mHTT* (A) but not in AAV-*wtHTT* injected animals (B). n = 45 (3 animals/ group).

(C-E) Densitometrical analysis revealed a significant loss of DARPP-32 protein (E) after 6 months of AAV-*mHTT* injection (D) compared to AAV-*wtHTT* animals (C). n = 12 (4 animals/ group).

(F-H) Striatal area measurements showed a significant decrease and ventricle area measurements showed a significant increase (H) between the AAV-*wtHTT* (F) and AAV-*mHTT* (G) injected animals after 6 months. n = 12 (4 animals/ group).

(I) Densitometrical analysis revealed a significant loss of DARPP-32 protein after 6 months of AAV-*mHTT* injection. n = 4 (4 animals/ group).

(J-K) NeuN staining in the AAV-*mHTT* (K) and AAV-*wtHTT* (J) injected animals after 6 months.

(L-O) IBA1 and GFAP staining show evidence for activated microglia and reactive astrocytes after 6 months in the AAV-*mHTT* (M and O) injected animals but not in the AAV-*wtHTT* (L and N).

(P-R) p62 and HTT accumulated and aggregated in the mHTT (Q and R) overexpressing animals compared to controls (P) at 6 months after injection.

(S-U) AGO2 did not accumulated in the mHTT overexpressing animals (T and U) compared to controls (S) at 6 months after injection.

(V) Relative p62 dot number and size was significantly increased in the mHTT overexpressing animals compared to controls at 6 months after injection. n = 24 (3 animals/ group).

(W) AGO2 accumulated but there was no significant difference in number in the mHTT overexpressing animals compared to controls at 6 months after injection. n = 24 (3 animals/ group).

(X) Densitometrical analysis revealed a significant increase of p62 protein after 6 months of AAV-*mHTT* injection. n = 4 (4 animals/ group).

(Y) Densitometrical analysis revealed a significant loss of AGO2 protein after 6 months of AAV-*mHTT* injection. n = 4 (4 animals/ group)

(Z) AGO2 protein level was significantly lower in HD post mortem striatal tissue (NIH NeuroBioBank) compared to healthy striatal tissue. n = 56 HD patients of different clinical grade (n = 12 grade 2, n = 34 grade 3, and n = 10 grade 4) and 31 age- and sex-matched controls.

WB values are normalized to AAV-*wtHTT* expression levels and corrected to Coomassie Brilliant Blue staining (I, X, and Y). WB values are normalized to CTRL expression levels and corrected to Ponceau S staining (Z). ***p<0.001; **p<0.01 ; *p<0.05; (A-Y) two-tailed two-sample unequal variance t-tests; (Z) non-parametric Kolmogorov-Smirnov test. All data are shown as mean ± SEM. Scale bars represents 50 μm (A, C, D, I, H, K, L, M, N, O , P, R and S), 1.5 mm (F and G), and 10 μm (Q and T).

Table S1. Colocalization Parameters. Related to Figure 3, 4, S3 and S5.

Figure ID	Colocalization Parameter	Range	Value	Colocalization %
Figure 3 F	Pearson's Coefficient	-1:1	0.1304±0.0096	13.04±0.96
Figure 3 F	Li's ICQ	-0.5:0.5	0.0648±0.0040	12.96±0.81
Figure 3 N	Pearson's Coefficient	-1:1	0.2614±0.0191	26.14±1.91
Figure 3 N	Li's ICQ	-0.5:0.5	0.1306±0.0042	24.50±0.83
Figure 4 D wtHTT	Pearson's Coefficient	-1:1	0.0448±0.0074	4.48±0.74
Figure 4 D wtHTT	Li's ICQ	-0.5:0.5	0.0187±0.0039	3.73±0.78
Figure 4 E mHTT	Pearson's Coefficient	-1:1	0.0884±0.0148	8.84±1.48
Figure 4 E mHTT	Li's ICQ	-0.5:0.5	0.0458±0.0074	9.16±1.49
Figure 4 I wtHTT	Pearson's Coefficient	-1:1	0.029±0.0034	2.9±0.34
Figure 4 I wtHTT	Li's ICQ	-0.5:0.5	0.0927±0.0080	18.53±1.6
Figure 4 J mHTT	Pearson's Coefficient	-1:1	0.039±0.0056	3.9±0.56
Figure 4 J mHTT	Li's ICQ	-0.5:0.5	0.1216±0.0105	24.32±2.1
Figure S3 S	Pearson's Coefficient	-1:1	0.1158±0.0161	11.58±1.61
Figure S3 S	Li's ICQ	-0.5:0.5	0.0470±0.0062	9.40±1.24
Figure S5 F mHTT	Pearson's Coefficient	-1:1	0.0616±0.0120	6.16±1.20
Figure S5 F mHTT	Li's ICQ	-0.5:0.5	0.0292±0.0087	5.85±1.73
Figure S5 G mHTT+BECN1	Pearson's Coefficient	-1:1	0.0339±0.0055	3.39±0.55
Figure S5 G mHTT+BECN1	Li's ICQ	-0.5:0.5	0.0110±0.0052	2.21±1.04

Table S2. Human samples. Related to Figure 3 and S5.

Figure 3 and Figure S5 ID	Brainbank ID	Age of death	Pathological Grade	Number of CAG repeats
Ctrl1	C572	59	-	-
Ctrl2	PT89	66	-	-
HD1	HD725	58	4	48
HD2	HD715	57	3	47
HD3	HD721	61	2	46

Table S3. Intrinsic membrane properties of medium-spiny neurons (MSN) from AAV-wtHTT and mHTT-injected animals. Related to Figure 1 and S2.

Whole-cell patch clamp recordings of medium-spiny neurons at 3 weeks after injection. 3 AAV-*mHTT* and 3 *wtHTT* injected animals included. There were no major differences in intrinsic membrane properties (i.e. resting membrane potential, cell capacitance, membrane resistance) or the frequency (Hz) of miniature Excitatory Postsynaptic Currents (mEPSC) between the groups. There was a small difference between the amplitude (pA) in mESPC however. The number of patched neurons (n) included in the analysis is written after the statistics in each case. N of action potentials (AP) represents the maximal number of spikes induced with currents in IV curve, (max 450 pA injected current). All data are shown as mean ± SEM. *p<0.05; two-tailed two-sample unequal variance t-tests.

Membrane intrinsic properties	**mHTT**	**wtHTT**	P<0,05
Resting membrane potentials (mV)	-80.75 ± 1.14, n = 12	-75.45 ± 2.53, n = 11	
Cell capacitance (pF)	88.62 ± 4.96, n = 13	100.6 ± 9.97, n = 13	
Input resistance (MΩ)	85.33 ± 10.58, n = 10	61.07 ± 10.46, n = 5	
Glutamatergic mEPSC (Hz)	3.07 ± 0.62, n = 11	2.84 ± 0.70, n = 8	
Glutamatergic mEPSC (pA)	11.57 ± 1.10, n = 11	7.94 ± 0.56, n = 8	*
No of AP	12.80 ± 0.82, n = 10	12.50 ± 0.34, n = 6	

Supplemental Experimental Procedures

Viral vectors

Lentiviral vectors were produced in 293T cells as previously described (Zufferey et al., 1997) and titrated by flow cytometry analysis and quantitative PCR analysis as previously described (Georgievska et al., 2004). The titers of the vectors used in this study were 2.83E+8 for wtHTT and 1.92E+9 TU/mL for mHTT. A MOI of 5 was used for transduction, vector stock was added to the medium, and 24 h later the vector containing media was replaced and changed to fresh culture media.

AAV vectors of serotype 5 encoding wtHTT, mHTT and mouse Beclin-1 were designed and produced as described before (Malmevik et al., 2015). The titer of the injected AAV-wtHTT, mHTT and BECN1 were 1.2E+15, 1.5E+15 and 6.15E+14 genome copies / ml, respectively. The final working dilution in PBS for each vector was 33 %.

Cell culture

All cell culture work on 293T cells was performed as described before (Musiwaro et al., 2013). Cells were grown in 24 well plates to ≈ 70 % confluence (for immunofluorescence) or ≈ 80 % confluence (for western blotting) in six well plates before any treatments were added. Mammalian phosphatidylinositol 3-kinase was blocked by the addition of 100 nM wortmannin (stock solution: 200 μM in DMSO, stored at –20 °C, Sigma-Aldrich) for 4 hours in the cell medium. Autophagosome maturation and lysosomal fusion was blocked using chloroquine (Sigma-Aldrich) at final concentrations of 100 μM (always fresh solution made in Milli-Q water) in normal cell medium also for 4 h (Musiwaro et al., 2013).

Electrophysiology

Patch-clamp electrophysiology was performed in mice that had been injected with AAV-*mHTT* or AAV-*wtHTT*. Mice were sacrificed 3 weeks after viral injection by an overdose of pentobarbital and brains were rapidly taken out and coronally cut on a vibratome at 275 μm in ice-cold Krebs buffer (gassed with 95 % O2 and 5 % CO2). Sections were

acclimatized for almost one hour in 37 °C solution before transferred to a recording chamber with continuous flow of Krebs solution gassed with 95 % O2 and 5 % CO2 at 28 °C. The composition of the Krebs solution for slice recording (and sectioning) was (in mM) 126 NaCl, 2.5 KCl, 1.2 NaH2PO4-H2O, 1.3 MgCl2-6H2O, and 2.4 CaCl2-6H2O. Recordings were made using Multi-clamp 700B (Molecular Devices), and signals were acquired at 10 kHz using pClamp10 software, data acquisition unit (Digidata 1440A, Molecular Devices). Access resistances were monitored throughout the experiments. Borosilicate glass pipettes (3–7 MOhm) for patching were filled with the following intracellular solution (in mM): 122.5 K-gluconate, 12.5 KCl, 0.2 EGTA, 10 Hepes, 2 MgATP, 0.3 Na3GTP and 8 NaCl adjusted to pH = 7.3 with KOH.
Cells in the mid-dorsal striatum were patched for recordings. Resting membrane potentials were monitored immediately after breaking-in, in current-clamp mode. For current-induced action potentials 500 ms currents were injected from -400 pA to +500 pA with 50 pA increments. Spontaneous postsynaptic activity was recorded in voltage-clamp mode at resting membrane potentials with 0.1 kHz in lowpass filter. Pure glutamatergic spontaneous events were distinguished by adding to the buffer tetrodotoxin (50 μM) that blocks action potentials via voltage-gated Na-channels and picrotoxin (1 μM) that blocks GABAergic activity via blockade of $GABA_A$ receptor.

Immunohistochemistry

At 3 weeks, 8 weeks or 6 months after injection all animals were trans-cardially perfused with ice cold 4 % PFA, and the brains then removed and post fixed overnight in 4 % PFA. Similarly, BACHD mice were perfused with PFA at 6 months of age. The following day, brains were put overnight in 25 % sucrose, frozen and then cut on a microtome into 30 or 35 μm sections in series of 6. Standard immunohistochemistry was applied to free-floating sections, as published in detail elsewhere (Malmevik et al., 2015). Primary antibodies were diluted as follows: mouse anti-HTT (EM48, 1:200, Millipore Cat# MAB5374 RRID:AB_177645), rabbit anti-DARPP-32 (1:500, Abcam Cat# ab40801 RRID:AB_731843), mouse anti-NeuN (1:1,000, Millipore Cat# MAB377 RRID:AB_2298772), rabbit anti-GFAP (1:1,000, Dako Cat# Z0334 RRID:AB_10013382), rabbit anti-IBA1 (1:1,000, Wako Cat# 019-19741 RRID:AB_2313566), rabbit p62 (1:500, Abcam Cat# ab91526 RRID:AB_2050336), rat

AGO2 (1:100, Sigma-Aldrich Cat# SAB4200085 RRID:AB_10600719), rabbit BECN1 (1:100, Santa Cruz Biotechnology Cat# sc-11427 RRID:AB_2064465), rabbit anti-LC3B (1:500, Novus Cat# NB100-2220 RRID:AB_10003146), rabbit LAMP1 (1:200, Sigma-Aldrich Cat# L1418 RRID:AB_477157), mouse anti-AGO2 (1:100, Sigma-Aldrich Cat#WH0027161M1, RRID:AB_1839441), rabbit anti-DCP1A (1:250, Abcam Cat# ab183709), rabbit anti-TIA1 (1:250, Abcam cat# ab140595). The dilution factor of the secondary antibodies was 1:200 (Jackson ImmunoResearch Labs Cat# 715-165-151 RRID:AB_2315777; Jackson ImmunoResearch Labs Cat# 711-485-152 RRID:AB_2492289; Jackson ImmunoResearch Labs Cat# 711-165-152 RRID:AB_2307443; Jackson ImmunoResearch Labs Cat# 712-225-153 RRID:AB_2340674). All fluorescent sections were counterstained with 4',6-diamidino-2-phenylindole (DAPI, Sigma-Aldrich, 1:1,000). For stainings in DAB, horseradish peroxidase conjugated secondary antibody (horse, Sigma-Aldrich, 1:400) was used.

We did a slightly modulated immunohistochemistry staining for mouse anti-HTT (EM48, 1:200, Millipore Cat# MAB5374 RRID:AB_177645) and rat anti-AGO2 (1:100, Sigma-Aldrich Cat# SAB4200085 RRID:AB_10600719) colocalization experiments. Firstly, sections were washed with KPBS and treated for 30 minutes with TRIS EDTA (pH = 9), then washed 2x with KPBS again before blocking and incubating with primary antibody diluted in serum overnight as published in detail elsewhere (Malmevik et al., 2015). The next day the sections were washed again 2x with KPBS and then biotinylated rabbit anti-rat secondary antibody (1:200, Vector Laboratories Cat# BA-4001, RRID:AB_10015300) was added for 2 hours together with regular rabbit anti-mouse Cy3 (1:200, Jackson ImmunoResearch Labs Cat# 315-165-003, RRID:AB_2340135). After washing the sections with KPBS, they were incubated for an hour with Alexa Fluor 488-Streptavidin antibody (1:200, Jackson ImmunoResearch Labs Cat# 016-540-084, RRID:AB_2337249) and then washed again with KPBS and mounted.

Staining of 10 μm thick paraffin-embedded sections from striatal HD - where the pathological severity was graded by an accredited neuropathologist according to the Vonsattel grading system (Vonsattel et al., 1985) - and healthy age-matched control brains using the above mentioned mouse anti-HTT, anti-AGO2 and anti-p62 antibodies were performed as described elsewhere (Drouin-Ouellet et al., 2015). Briefly: sections were

dried at 65 °C for 10 minutes, surrounded with Dakopen and incubated first with xylene and then with different concentrations of ethanol (99.5 %, 95 %, 70 %), MilliQ water and last in TN buffer (1 M TRIS-HCl, 1.5 M NaCl, MilliQ water) before 20 minutes boiling in a pH = 9 TRIS/ EDTA solution. After cooling, the sections were incubated, again twice, with TN buffer and then with TN + 5 % serum in RT. After these steps the primary antibody was diluted in TNT + 5 % serum (TN + 10 % Tween20) and the sections were incubated at RT. After washing with TN and TNT, secondary antibodies were diluted in TNT + 5 % serum and kept in the dark for 2 hours. Sections were washed, mounted and cover slipped with PVDA-DABCO with DAPI. All fluorescent images were taken using a Leica TCS SP8 confocal laser scanning microscope.

Immunocytochemistry and high-content screening

For high-content screening (HCS) all cells (treated or not treated) were fixed in 24 well plates with 4 % PFA for 15 minutes, followed by two washing steps with PBS. Staining was performed as previously described (Sachdeva et al., 2010; Thompson et al., 2005). Primary anti-mouse p62 (Abcam Cat# ab56416 RRID:AB_945626) antibody was diluted at 1:500. Cy-2 secondary antibody was used in 1:200 (Jackson ImmunoResearch Labs Cat# 715-545-150 RRID:AB_2340846). All fluorescent labelings were counterstained with DAPI. Average p62 dot number and size / well was measured with a Thermo Scientific Cellomics ArrayScan VTI HCS Reader. The cells nuclei were defined by DAPI (Sigma-Aldrich, 1:1,000), the cytoplasm was measured as a ring around the nuclei and p62 dots were detected (with Spot Detection) and measured in each case.

Western Blot

For western blots on 293T cells, the medium was removed from the 6-well plates and the differentially treated cells were lysed in RIPA buffer (Sigma-Aldrich) supplemented with Protease inhibitor cocktail (PIC, Complete, 1:25) for 2 - 3 minutes. The cells were scraped off the well and transferred to tubes for incubation on ice for 30 minutes. Afterwards cells were centrifuged at 10,000 x g for 10 minutes at 4 °C. The supernatants were collected and transferred to a new tube and stored at - 20 °C.

For western blots from fresh striatal tissue, injected mice were sacrificed by cervical

dislocation and the striatum was dissected and transferred to an eppendorf tube with a magnetic bead (Qiagen) and kept on dry ice. 150 µl RIPA + PIC was added. The samples were put in TissueLyser LT (Quiagen) on 50 Hz for 2 minutes, twice, and then put back on ice until most of the foam disappeared. The homogenized samples were transferred to a new tube and stored at – 20 °C.

Protein concentration was determined using a DC protein assay kit (Bradford method). 15 – 30 µg of protein was boiled at 95 °C for 5 minutes in Laemmli buffer (BioRad) and separated on a 4 – 12 % SDS/PAGE gel. SDS-PAGE gels loaded with 6 months AAV-*wtHTT* and *mHTT* striatal samples were first stained with Coomassie Blue for 4 hours, then de-stained for 24 hours in 5 % methanol + 7.5 % acetic acid solution. Gels were then electro transferred either using the Transblot®-Turbo™ Transfer system (BioRad) or using Xcell II™ Blot module (Invitrogen) at 100 V, for 1 hour on a PVDF membrane. Membranes were incubated in Ponceau S solution for 15 minutes and washed with water for at least 1 hour. After blocking for 1 hour in Tris-buffered saline with 0.1 % Tween20 (TBST) and 5 % (wt/vol) nonfat dry milk, membranes were incubated overnight at 4 °C. The following primary antibodies were used: mouse anti-AGO1 (1:1,000, Abcam Cat# ab98056, RRID:AB_10680548), rabbit anti-DARPP-32 (1:50,000, Abcam Cat# ab40801 RRID:AB_731843), rabbit anti-LC3B (1:5,000, Novus Cat# NB100-2220 RRID:AB_10003146), mouse anti-LAMP1 (1:250, Santa Cruz Biotechnology Cat# sc-17768 RRID:AB_626851), mouse anti-p62 (1:5,000, Abcam Cat# ab56416 RRID:AB_945626), rat anti-AGO2 (1:1,000, Sigma-Aldrich Cat# SAB4200085 RRID:AB_10600719), rabbit BECN1 (1:1,000, Santa Cruz Biotechnology Cat# sc-11427 RRID:AB_2064465), mouse anti-AGO2 (1:1,000, Sigma-Aldrich Cat#WH0027161M1, RRID:AB_1839441), rabbit anti-TIA1 (1:2,500, Abcam cat# ab140595). After washing twice for 15 minutes in TBST, membranes were incubated for 1 hour at room temperature with HRP-conjugated secondary antibodies: anti-rabbit (1:2,000, GE Healthcare), anti-rat (1:10,000, Jackson ImmunoResearch Labs Cat# 712-035-153 RRID:AB_2340639) or anti-mouse (1:5,000, Santa Cruz Biotechnology Cat# sc-2005 RRID:AB_631736). Actin staining was done using a monoclonal mouse anti-β-actin HRP (1:50,000, Sigma-Aldrich Cat# A3854 RRID:AB_262011) in blocking solution. Protein expression was revealed with the ECL™ Prime Western Blotting Detection Reagent (Life technologies). Signal was detected using a Chemidoc MP system (BioRad) and band intensities were quantified

by densitometry using the ImageJ software.

Quantitative real-time PCR

To measure the expression level of different miRNAs and RNAs animals were first injected with AAV-*wtHTT* or *mHTT* and sacrificed 3 weeks after injection. Striatal tissue was quickly dissected after cervical dislocation and homogenized in an eppendorf tube in QIAzol Lysis Reagent with a magnetic bead (Qiagen) using a TissueLyser (30 Hz, 2 x 2 minutes). miRNA and total RNA was extracted according to the supplier's recommendations using the mini miRNeasy kit (Qiagen).

cDNA was generated from five AAV-*wtHTT* and five AAV-*mHTT* injected animals using the Maxima First Strand cDNA Synthesis Kit for qRT–PCR. All primers were used together with LightCycler 480 SYBR Green I Master (Roche). Two reference genes were used for each qPCR analysis (ACTB and GAPDH). AGO2, AGO1 and AGO4 primer sequence were:

AGO2 fw: TAAATACGCACAGGGTGCAG

AGO2 rev: TCTGCACGTTCTTCATCTGG

AGO1 fw: CAATCAAGCTTCTGGCCAAT

AGO1 rev: AGATCTGCGGTTTGAAATGC

AGO4 fw: AAAGTATGGGCAGTGGCTTG

AGO4 rev: TGCACCTTGAGCATACTTGC.

To synthesize cDNA from miRNA we used the Universal cDNA synthesis kit (Exiqon). miRCURY LNA™ PCR primer sets, SNORD65, SNORD-68, hsa-miR-9, hsa-miR-125 and hsa-miR-21 were purchased from Exiqon. SYBR green qRT–PCR was performed. Relative enrichment of genes was calculated using SNORD65 and SNORD68 as controls. In all cases data were quantified using the $\Delta\Delta C_t$ method.

Colocalization analysis

All pictures for colocalization analysis were taken with confocal microscope using the same magnification and settings in 2-3 sections from 3-3 animals per group. Pictures were transferred to ImageJ and colors were splitted first. JACoP: Just Another Colocalization Plugin was used for image analysis (https://imagej.nih.gov/ij/plugins/track/jacop2.html)

(Bolte and Cordelières, 2006). In order to determine colocalization between AGO2 - p62, AGO2 – DCP1A or AGO2 – TIA1 two independent methods were used for imaging data analysis. First Pearson's coefficient was determined. Second, Li's intensity correlation analysis was performed to gain further insight into the degree of colocalization. This method calculates the difference from the mean channel intensity for each color at each pixel. Li's intensity correlation analysis was also used to define Li's intensity correlation quotient (ICQ). Colocalization parameters were summarized in Table S1 with % colocalization defined by Pearson's coefficient x 100 or Li's ICQ x 2 x 100. All data are shown as mean ± SEM.

Analysis of in vivo mouse small RNA-seq data

The 50 bp single end reads were mapped to the mouse genome (mm10) using STAR_2.4.0j (Dobin et al., 2013). Reads mapping to miRNAs were quantified with FeatureCounts (Liao et al., 2014) using annotation files from miRbase (www.miRbase.org (Kozomara and Griffiths-Jones, 2014)), counting only primary reads. For differential expression analyses (Bioconducter/R package DESeq2) and the identification of miRNA families, data was normalized to the total read number mapping to the genome. MiRNA families were identified based on miRbase annotations (www.miRbase.org (Kozomara and Griffiths-Jones, 2014)).

To investigate relative miRNA levels, reads mapping to miRNAs in *mHTT* and *wtHTT* injected animals were normalised to the total number of reads mapping to tRNAs. tRNA annotations were obtained from UCSC Repeat Masker Track (Kersey et al., 2016). wtHTT miRNA levels were used as reference.

The small RNA-seq data from this publication has been submitted to the NCBI Gene Expression Omnibus database and assigned the GEO series accession number GSE78928.

Analysis of in vitro small RNA-seq data in 293T cells

Previously harvested transduced 293T cells (miRNAEasy kit, Quiagen) were sent for small RNA-seq to the Clinical Microarray Core (University of California, Los Angeles [UCLA], CA, USA) (n = 6).

The 50 bp single end reads were mapped to the genome (hg19). Reads were quantified to

miRBase (ADD REF). For differential expression analyses (Bioconducter/R package DESeq2) data was normalized to the total read number mapping to the genome.
To investigate relative miRNA levels, reads mapping to miRNAs in mHTT and wtHTT samples were normalised to the total number of reads mapping to repeats obtained from UCSC Repeat Masker Track. wtHTT miRNA levels were used as reference.
The small RNA-seq data from this publication have been submitted to the NCBI Gene Expression Omnibus database and assigned the GEO series accession number GSE78928.

RNA-seq and analysis

Previously harvested transduced 293T cells (miRNAEasy kit, Quiagen) were sent for mRNA-seq to the Clinical Microarray Core (University of California, Los Angeles [UCLA], CA, USA) (n = 6).

For striatal samples, the striatum was quickly dissected from decapitated vector-injected mice (n = 6), frozen on dry ice and homogenised in Tissue LyserLT (50 Hz, 2 x 2 min). Total RNA was extracted using the miRNeasy mini kit (Qiagen).
The 50 bp single end reads were mapped to the genome (mm10 for mouse striatal tissue and hg19 for 293T cells). Reads were quantified to Refseq. The normalisation and identification of differentially expressed genes was conducted using the Bioconducter/R package DESeq2.
The RNA-seq data from this publication have been submitted to the NCBI Gene Expression Omnibus database and assigned the GEO series accession number GSE78928.

miRNA target analysis

TargetScan (release 7.1, June 2016), was applied to get predicted targets of let-7, miR-9 and miR-128 (Agarwal et al., 2015). All targets with a cumulative weighted context score < 0 was used in the analysis. We also applied a list of potential miR-128 targets as predicted by AGO2 HITS-CLIP-seq in Camk2a neurons, taking all genes with perfect base pairing of at least 6 nucleotides between miR-128 target sequence and the 3'UTR of AGO2-associated genes (Tan et al., 2013). To remove noise from low expressing transcripts, we only included genes with >16 sequencing reads on average through the

samples. Venn plots were generated using the R package VennDiagram (Hanbo, 2014). The R package DESeq2 (Love et al., 2014) was used to calculate fold changes of genes. Gene ontology enrichment analysis was performed using the online resource of the Gene Ontology Consortium (http://geneontology.org/page/go-enrichment-analysis (Gene Ontology, 2015), with the Panther classification system (Mi et al., 2016). Upregulated genes were defined as genes with $\log_2$ fold change > 0.1 and p-value < 0.05. This list was tested against a reference background list with all expressed genes (>16 reads) in the samples.

For miRNA target analysis related to Figure S5I we first assessed genes targeted by miRNAs that were not expressed in our samples in Figure S5I. We identified two miRNAs that were completely absent in our AAV-*wtHTT* or *mHTT* injected animals, miR-302 and miR-486. However, many target genes of these two miRNAs are redundantly targeted by other miRNAs that are highly expressed in our samples and will therefore be affected by inactivation of those expressed miRNAs. For example: miR-302 alone has 1003 predicted target genes. However, 949 of these genes are targeted by at least one other miRNA that has more than 200 reads. To overcome this issue, we included only miR-302 and miR-486 targets that were not targeted by any other expressed (>200 reads) miRNA. We repeated the same analysis for miR-486 and found that the fold-change distribution of target genes does not show a shift to de-repression as seen with target genes of let-7, miR-9 and miR-128; instead, they are significantly shifted in the opposite direction, suggesting these genes are not affected (Figure S5I; pink and green lines).

As an additional control, we analysed all genes that were not targeted by any expressed miRNA. We found 250 miRNAs with >200 reads in the brain samples. We identified 1704 target mRNAs that were not directly targeted by any of these highly expressed miRNAs (Figure S5I; orange line of the plot). We have also identified miRNA target genes of non–expressed miRNAs (1021 miRNAs) in neurons where we also removed targets of the highly expressed miRNAs >200 reads, leaving 543 genes not targeted by any highly expressed miRNA in our samples (Figure S5I; red line of the plot). These 543 miRNA-targets show no trend of de-repression, such as the target genes of let-7, miR-128 and miR-9. Taken together, in all analyses of target genes of non-expressed miRNAs there is no evidence for target de-repression like the target genes of highly expressed miRNAs (let-7,

miR-128 and miR-9).

Statistical analysis

The intensity of DARPP-32 expression in the striatum was measured on 3 representative sections from each brain using ImageJ. In each case the contralateral, non-injected site was used for normalization.

Amounts of HTT inclusion bodies were quantified by counting the dots in a 1 mm^2 sized area around the needle track in 3 representative sections from each brain.

Striatal and ventricular volumes from animals injected 8 weeks or 6 months previously were measured and calculated with ImageJ. For both wt and mHTT injected animals representative sections were measured from each brain. In all cases the contralateral, non-injected site was used for normalization.

Relative p62, TIA1, LAMP1 and AGO2 dot number and size were defined with ImageJ as previously described (Pircs et al., 2012). All pictures taken with the confocal microscopy were done using a magnification of 20x or 63x. Pictures of AGO2, TIA1, LAMP1 or p62 stainings were taken with the same settings. Pictures were transferred to ImageJ, converted into black and white and dots were defined by setting the same threshold for each staining. The amount of dot number and area was measured in each case in 3-3 sections per brain in at least 3-3 animals per staining. Values were measured in each case in the same area defined in ImageJ and then normalized to the control conditions giving a relative dot number/ area or dot size/ area.

The percentage of p62 or AGO2 cell numbers were counted manually based on DAPI staining in ImageJ. All pictures with confocal microscopy were done using a magnification of 63x. Pictures of AGO2 or p62 staining were taken with the same settings. Pictures were transferred to ImageJ, converted into black and white and AGO2 or p62 positive cell counts were defined by setting the same threshold for each staining. Values were measured in each case in the same area defined in ImageJ and then normalized to the cell number for each picture.

Supplemental References

Agarwal, V., Bell, G.W., Nam, J.W., and Bartel, D.P. (2015). Predicting effective microRNA target sites in mammalian mRNAs. eLife *4*.

Bolte, S., and Cordelières, F.P. (2006). A guided tour into subcellular colocalization analysis in light microscopy. J Microsc *224*, 213-232.

Dobin, A., Davis, C.A., Schlesinger, F., Drenkow, J., Zaleski, C., Jha, S., Batut, P., Chaisson, M., and Gingeras, T.R. (2013). STAR: ultrafast universal RNA-seq aligner. Bioinformatics *29*, 15-21.

Drouin-Ouellet, J., Sawiak, S.J., Cisbani, G., Lagace, M., Kuan, W.L., Saint-Pierre, M., Dury, R.J., Alata, W., St-Amour, I., Mason, S.L., *et al.* (2015). Cerebrovascular and blood-brain barrier impairments in Huntington's disease: Potential implications for its pathophysiology. Annals of neurology *78*, 160-177.

Gene Ontology, C. (2015). Gene Ontology Consortium: going forward. Nucleic acids research *43*, D1049-1056.

Georgievska, B., Jakobsson, J., Persson, E., Ericson, C., Kirik, D., and Lundberg, C. (2004). Regulated delivery of glial cell line-derived neurotrophic factor into rat striatum, using a tetracycline-dependent lentiviral vector. Human gene therapy *15*, 934-944.

Hanbo, C. (2014). VennDiagram: Generate high-resolution Venn and Euler plots.

Kersey, P.J., Allen, J.E., Armean, I., Boddu, S., Bolt, B.J., Carvalho-Silva, D., Christensen, M., Davis, P., Falin, L.J., Grabmueller, C., *et al.* (2016). Ensembl Genomes 2016: more genomes, more complexity. Nucleic acids research *44*, D574-D580.

Kozomara, A., and Griffiths-Jones, S. (2014). miRBase: annotating high confidence microRNAs using deep sequencing data. Nucleic acids research *42*, D68-D73.

Liao, Y., Smyth, G.K., and Shi, W. (2014). featureCounts: an efficient general purpose program for assigning sequence reads to genomic features. Bioinformatics *30*, 923-930.

Love, M.I., Huber, W., and Anders, S. (2014). Moderated estimation of fold change and dispersion for RNA-seq data with DESeq2. Genome biology *15*, 550.

Malmevik, J., Petri, R., Klussendorf, T., Knauff, P., Akerblom, M., Johansson, J., Soneji, S., and Jakobsson, J. (2015). Identification of the miRNA targetome in hippocampal neurons using RIP-seq. Scientific reports *5*, 12609.

Mi, H., Poudel, S., Muruganujan, A., Casagrande, J.T., and Thomas, P.D. (2016). PANTHER version 10: expanded protein families and functions, and analysis tools. Nucleic acids research *44*, D336-342.

Musiwaro, P., Smith, M., Manifava, M., Walker, S.A., and Ktistakis, N.T. (2013). Characteristics and requirements of basal autophagy in HEK 293 cells. Autophagy *9*, 1407-1417.

Pircs, K., Nagy, P., Varga, A., Venkei, Z., Erdi, B., Hegedus, K., and Juhasz, G. (2012). Advantages and limitations of different p62-based assays for estimating autophagic activity in Drosophila. PloS one *7*, e44214.

Sachdeva, R., Jonsson, M.E., Nelander, J., Kirkeby, A., Guibentif, C., Gentner, B., Naldini, L., Bjorklund, A., Parmar, M., and Jakobsson, J. (2010). Tracking differentiating neural progenitors in pluripotent cultures using microRNA-regulated lentiviral vectors. Proceedings of the National Academy of Sciences of the United States of America *107*, 11602-11607.

Tan, C.L., Plotkin, J.L., Veno, M.T., von Schimmelmann, M., Feinberg, P., Mann, S., Handler, A., Kjems, J., Surmeier, D.J., O'Carroll, D.*, et al.* (2013). MicroRNA-128 governs neuronal excitability and motor behavior in mice. Science *342*, 1254-1258.

Thompson, L., Barraud, P., Andersson, E., Kirik, D., and Bjorklund, A. (2005). Identification of dopaminergic neurons of nigral and ventral tegmental area subtypes in grafts of fetal ventral mesencephalon based on cell morphology, protein expression, and efferent projections. The Journal of neuroscience : the official journal of the Society for Neuroscience *25*, 6467-6477.

Vonsattel, J.P., Myers, R.H., Stevens, T.J., Ferrante, R.J., Bird, E.D., and Richardson, E.P., Jr. (1985). Neuropathological classification of Huntington's disease. Journal of neuropathology and experimental neurology *44*, 559-577.

Zufferey, R., Nagy, D., Mandel, R.J., Naldini, L., and Trono, D. (1997). Multiply attenuated lentiviral vector achieves efficient gene delivery in vivo. Nature biotechnology *15*, 871-875.